Analysis on Governing Processes of Mixed Layer Depth Variability in the Labrador Sea

By

HyunJin Park

in partial fulfilment of the requirements for the degree of

Master of Science
in Civil Engineering

at the Delft University of Technology,
to be defended publicly on Tuesday November 26, 2019 at 11:00 AM.

Supervisor:	Dr. C.A. Katsman	
Thesis committee:	Dr. J.M. Sayol,	TU Delft
	Dr. S.R. de Roode,	TU Delft

TU Delft

Abstract

As a key component to the bottom limb of the Atlantic Meridional Overturning Circulation (AMOC), the Labrador Sea is one of the regions where deep ocean convection takes place. This convection is driven by atmospheric cooling during winter, which brings the surface water into the intermediate and deep layers by uniformizing water mass properties. This homogeneous layer is called Mixed Layer (ML). As a result of this convection, stratification is no longer maintained, and the Mixed Layer Depth (MLD) deepens. During this deepening, an enormous amount of potential energy is converted to kinetic energy, and meso- and sub-mesoscale instabilities develop.

After wintertime, the MLD starts to shallow again. Atmospheric-induced convection ceases or decreases significantly and physical components return to stratified conditions. Baroclinic instabilities grown to mesoscale or geostrophic scale play a role in restratifying the ML through the formation of coherent ocean eddies. This chain of processes follows a seasonal cycle that strongly depends on the imbalance between horizontal and vertical buoyancy gradients. A practical way to quantify this imbalance is the use of the Ertel potential vorticity or a derived magnitude as the Richardson angle, which allow to infer the existence of instabilities and to classify them respectively.

This study analyzes the physical processes behind the MLD seasonal variability in the Labrador Sea. To this end, high-resolution model data (1/12° × 1/12°) from a global simulation has been used. An evaluation of spatial and temporal patterns of the MLD and energy conversion is provided, and the dominant types of instabilities are determined. It is hypothesized that these instabilities drive the energy conversion and the growth of coherent mesoscale eddies, which can modify the MLD and restratify the ocean. Finally, the sequential interactions among the processes are investigated to provide better understanding about seasonal MLD variability.

This study shows that the density-based MLDs with a threshold of $\Delta\sigma_\theta = 0.03\ kg\ m^{-3}$ are the most credible values, and the spatial and temporal patterns of energy conversion and gravitational/symmetric instabilities are in phase with the MLD variability. The energy conversion is investigated by means of the available potential energy (APE), kinetic energy (KE) and Energy Ratio (ER) which is introduced in this study, and a large amount of gravitational and/or symmetric instabilities is found within ML, especially in the upper ocean layers. The role of baroclinic instabilities is investigated with the Eady growth rate, while the presence of coherent mesoscale eddies is inferred from the Okubo-Weiss parameter and the Eddy Kinetic Energy, whose size is limited by the internal Rossby radius. This study shows that the MLD variability is the result of changes in the conversion between the available potential energy (APE) and kinetic energy (KE) as well as of the competition between gravitational/symmetric and baroclinic instabilities. The former favoring MLD deepening, and the latter favoring MLD shallowing.

Contents

List of Figures

List of Tables

1. Introduction

1.1 Context

As a key component to the bottom limb of the Atlantic Meridional Overturning Circulation (AMOC), the Labrador Sea is one of the regions where deep ocean convection takes place (Georgiou et al. 2019). This convection is driven by strong cooling in contact with the atmosphere during winter, which brings cold and fresh water into the intermediate water depth and uniformizes physical properties, such as potential temperature, salinity, potential density, oxygen contents or bio-substances. This homogeneous layer is called the Mixed Layer (ML) and is considered as an evidence of vigorous turbulent mixing. As a result of this convection, stratification is no longer maintained, and the Mixed Layer Depth (MLD) deepens, reaching depths over 1000m at some regions. During this deepening, a large amount of energy is converted from potential to kinetic energy and mesoscale and submesoscale instabilities develop. Submesoscale instabilities are the source of these mixing processes, while mesoscale instabilities try to put back the system into the previous state.

After wintertime, atmospheric-induced convection ceases and the ML starts to restratify thus reducing the MLD. Baroclinic instabilities developed at mesoscale or geostrophic scale (from tens to hundreds of km) play a role in restratifying the ML by generating eddies in the ocean. This chain of processes (mixing and stratifying) follows a seasonal cycle that strongly depends on the imbalance between horizontal and vertical buoyancy gradients, such as the absolute and planetary vorticity, the buoyancy gradient or the current shear. A practical way to quantify this imbalance is the use of the Ertel potential vorticity or a derived magnitude as the Richardson angle, which allow to infer the existence of instabilities and to classify them respectively.

1.1.1 Labrador Sea

The Labrador Sea is part of the North Atlantic Ocean, located between the Labrador Peninsula and Greenland. The sea is surrounded by continental shelves and connected in the south with the open Atlantic Ocean and in the east with the Nordic Seas via the Irminger Sea. The Labrador Sea has been described as a marginal sea of the Atlantic (Spall 2004, Calow 2009).

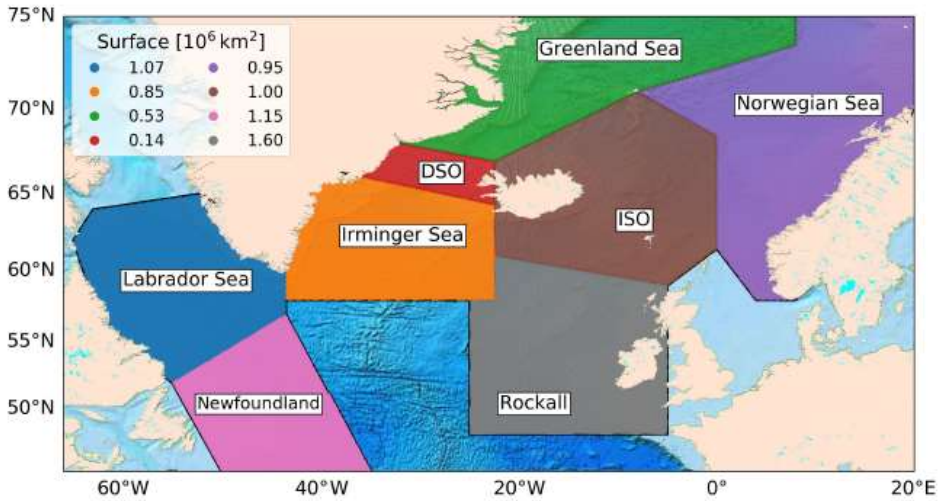

Figure 1.1 Map of the subpolar North Atlantic in which the different seas are displayed with color shading. Surface areas are denoted in the legend (Sayol et al. 2019).

During winter, the Labrador Sea experiences enhanced air-sea heat loss driven by cold airflows over the Labrador Sea and develops a convectively mixed surface layer whose depth depends on the magnitude of buoyancy loss (Curry et al. 1998, Pickart et al. 2002). When the depth of convection is large enough, a distinct layer of minimum vertical density gradient appears. This unique water mass is known as Labrador Sea Water (LSW) (Lazier et al. 2002). The convective mixed layer depth may reach even more than 2000m depending on the severity of the winter.

Deep convection in the Labrador Sea provides an important pathway for atmospheric gases, heat, salinity, bio and chemical substances from the surface mixed layer to intermediate depths (Pickart et al. 1997, Sy et al. 1997, Lavender et al. 2000). The convected LSW flows into the Labrador's surrounding ocean, and it transports fluxes and tracers to the open ocean, thus ventilating deeper layers (Lazier et al. 2002). In order to investigate the large variability of LSW production, the Bedford Institute of Oceanography has surveyed on a line of CTD stations across the Labrador Sea in the early summers of each year since 1990 (Figure 1.2 left panel).

An example of salinity distribution along the CTD line is presented in Figure 1.2 (right). The nearly homogeneous LSW between 500–2300m and between 360–800 km was generated by deep convection during the previous winter. The layer above 500m of the water is less well mixed and has lower salinity than the deeper layer. This is because more saline water from the Irminger Sea is transported into the Labrador Sea by the Irminger and the West Greenland currents (Figure 1.2 left). In the west, another saline water mass is observed at about 300m over the shelf (Figure 1.2 right). This corresponds to Irminger Water transported through the Labrador Sea by the West Greenland and Labrador currents. Another feature is that there is fresh water mass on a shelf in the west, which comes from the Davis Strait (Lazier et al. 2002).

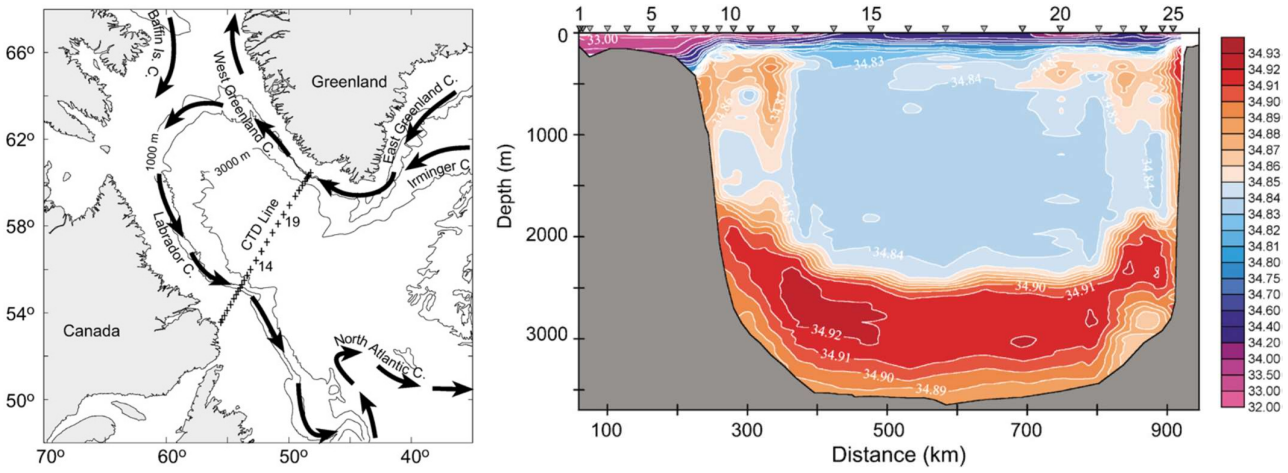

Figure 1.2 Map of the Labrador Sea and the Labrador, North Atlantic and West Greenland Currents (left) and salinity distribution along the CTD line obtained between 19 and 23 June 1993 (right) (Lazier et al. 2002).

1.1.2 Dataset

The dataset analyzed in this study is a subset from a control run by the Parallel Ocean Program (POP) (Brunnabend et al. 2017), also used by Sayol et al. (2019), courtesy of Nils Brüggemann. The POP solves the primitive equations on a tri-polar curvilinear grid, and the bottom topography is described by partial bottom cells (Adcroft et al. 1997), and Figure 1.3 shows the model bathymetry. An annual cycle from the Coordinated Ocean Reference Experiment (CORE) forcing dataset was applied for the atmospheric forcing (wind, heat fluxes and precipitation), and observed river run-off was also included in the model. Hence, inter-annual and longer time scales of variability are excluded from the forcing. One year of daily averaged data is used in this study. Original curvilinear horizontal grid data has been interpolated using a bi-linear interpolation to a regular

mesh of 1/12° × 1/12°. Figure 1.4 shows the schematization of model configuration and dataset, and Table 1.1 presents the key parameters applied in the model.

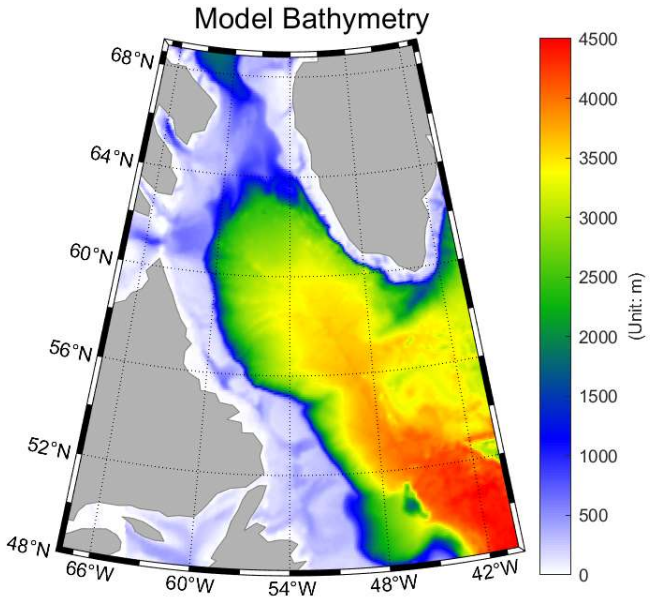

Figure 1.3 Model bathymentry.

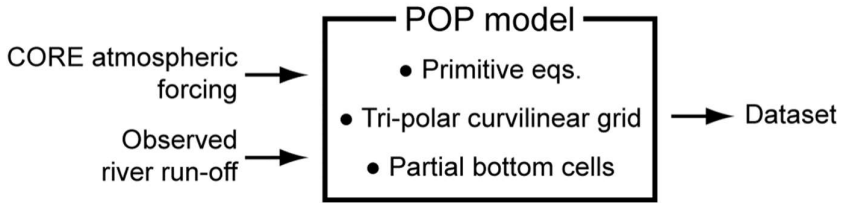

Figure 1.4 Schematization of model configuration and dataset.

Parameter	Value
Horizontal resolution	0.1° at the equator
Vertical resolution	42 non-equidistant z-levels. From 10 m (surface) to 250 m (deepest)
Horizontal dissipation (momentum)	Bi-harmonic viscosity and diffusion ∝ grid size^3. At the equator υ_0 = -90m^4/s
Horizontal dissipation (tracers)	Bi-harmonic viscosity and diffusion ∝ grid size^3. At the equator k_0 = -30m^4/s
Vertical Mixing (K-profile)	0.1m^2/s to solve gravitational instabilities
Background vertical tracer diffusion	From 10^{-5}m^2/s (surface) to 10^{-4}m^2/s (depth)

Table 1.1 Summary of POP model key parameters used in the simulation (Sayol et al. 2019).

The dataset consists of eight variables: longitude and latitude coordinates (with 1/12° × 1/12° of spatial resolution after interpolation), depth (42 layers) and three-dimensional current velocities (u, v, w), salinity (S)

and potential temperature (θ). Table 1.2 shows the definition and dimension of these variables, and Figure 1.5 shows the example data for the surface salinity and the surface potential temperature.

Variable	Definition (Unit)	Dimension
x	Longitude (°W)	68°W ~ 39.92°W, Δx = 1/12°, N_x = 338
y	Latitude (°N)	48°N ~ 69°N, Δy = 1/12°, N_y = 253
z	Depth (m)	5m ~ 5875m, Δz = 10~250m, N_z = 42
u	Zonal (x direction) velocity component (m/s)	N_x = 338 × N_y = 253 × N_z = 42
v	Meridional (y direction) velocity component (m/s)	N_x = 338 × N_y = 253 × N_z = 42
w	Vertical (z direction) velocity component (m/s)	N_x = 338 × N_y = 253 × N_z = 42
S	Salinity (PSU)	N_x = 338 × N_y = 253 × N_z = 42
θ	Potential temperature (°C)	N_x = 338 × N_y = 253 × N_z = 42

Table 1.2 Summary of dataset variables used in this study.

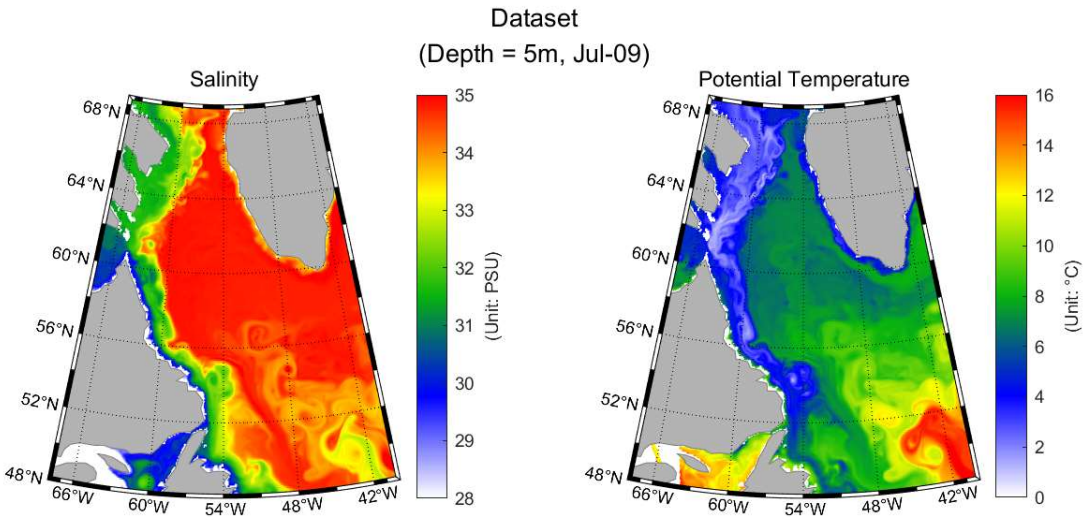

Figure 1.5 Surface salinity and surface potential temperature of the dataset at the 190th time step (July 9th).

1.2 Mixed Layer Depth

The ML is the upper part of the ocean where active air–sea exchanges develop surface turbulence and mixing which generate vertically uniform water mass and low gradients in temperature, salinity and density. Within the upper layer, several distinct layers formed by different spatio-temporal processes can be distinguished that are formed over different timescales: the upper mixed layer, seasonal pycnocline, and the permanent pycnocline (Figure 1.6).

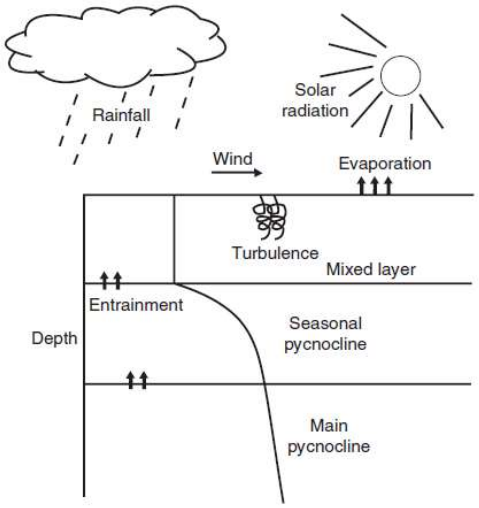

Figure 1.6 Conceptual diagram of the vertical structure of the ocean upper layers (Sprintall et al. 2018).

Although an accurate measurement of the MLD can be provided through direct measurements of turbulence in the upper layer, turbulent scales are small and hard to detect. For this reason, criteria to define the MLD are generally based on temperature, salinity or density. The MLD must define the depth of the transition from a homogeneous upper layer to the stratified layer (Sprintall et al. 2018).

This transition is arbitrary as it depends on the threshold considered and can differ between properties and time scales (e.g., day, month). Various criteria have been suggested in previous studies, and Table 1.3 gives an example of that using the threshold method, for which the MLD is the depth at which temperature or potential density changes by a given threshold value relative to the one at a near-surface reference depth.

Author and Area Studied	**MLD Threshold Criterion**	**Z_{ref}**
Kara et al. (2000b), Global Ocean	$\Delta T = 0.8℃$ $\Delta\sigma_\theta = \sigma_\theta(T + \Delta T) - \sigma_\theta(T)$ with $\Delta T = 0.8℃$	10 m
Monterey and Levitus (1997), Global Ocean	$\Delta T = 0.5℃$ $\Delta\sigma_\theta = 0.125\ \mathrm{kg}\ m^{-3}$	0 m
Obata et al. (1996), Global Ocean	$\Delta T = 0.5℃$	0 m
Spall et al. (2000), North Atlantic	$\Delta T = 0.5℃$	0 m

Table 1.3 Examples of criteria used to define the MLD from a threshold method for the North Atlantic. Z_{ref} is a reference depth and ΔT and $\Delta\sigma_\theta$ are temperature-based and density-based threshold values (de Boyer Montégut et al. 2004).

de Boyer Montégut et al. (2004) analyzed about 4 million hydrographic profiles from the National Oceanographic Data Center and the World Ocean Circulation Experiment database and reviewed various threshold values for MLD criterion by a visual inspection. Their reference depth was set at 10 m to avoid the diurnal cycle of the surface layer because a density threshold of 0.03 kg m^{-3} with a reference depth of 2.5 m is known to yield the mixing layer under the strong diurnal cycle (Schneider et al. 1990), and temperature variations can reach 1 or 2°C within the first 1–2 m under light winds and solar warming (Price et al. 1986).

In order to select appropriate threshold values, they computed MLDs based on various temperature and density criteria for all profiles and took a visual inspection for randomly picked profiles with a global coverage of all seasons. Their analyses for the profiles show that a threshold value of 0.01 kg m^{-3} provides rather shallow MLDs (Brainerd et al. 1995), and the threshold values 0.1 kg m^{-3} and 0.05 kg m^{-3} often yielded the depth of the main thermocline or seasonal thermocline rather than at its top. Hence, they concluded that the

threshold value 0.03 kg m^{-3} is a more appropriate value for the density criterion. In a similar way, they decided that the threshold value of 0.2°C is a suitable threshold for temperature because a difference of 0.1°C corresponds to a smaller density criterion than 0.01 kg m^{-3}, and often yields the mixing layer depth rather than MLD.

In terms of reduction of the data, they interpreted that the median is a more appropriate estimator than the mean of the MLDs for a single location as MLDs often tend to be skewed to higher values (Figure 1.7c for the ΔT = 0.2°C criterion). They also analyzed that the MLDs computed with the averaged profiles are approximately 25% shallower than those based on individual profiles (see Figure 1.7).

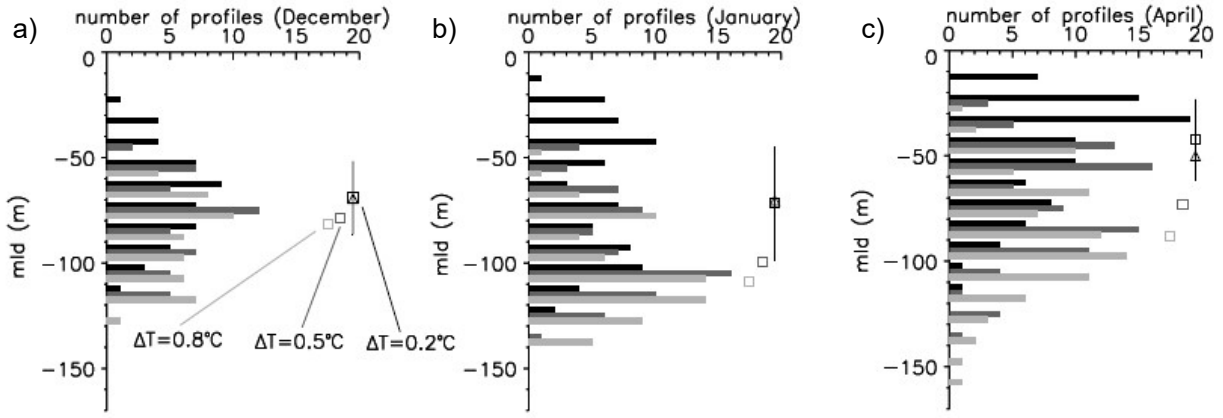

Figure 1.7 Distribution of MLDs located in the subtropical North Pacific for three selected months: December (panel a), January (panel b), and April (panel c). The three MLD criteria are ΔT = 0.2°C (black), 0.5°C (dark gray shading), and 0.8°C (light gray shading) from 10 m reference depth. The median (squares) is indicated for all temperature thresholds, while the median average deviation (vertical bars) and the mean (triangles) are only depicted for ΔT = 0.2°C (de Boyer Montégut et al. 2004).

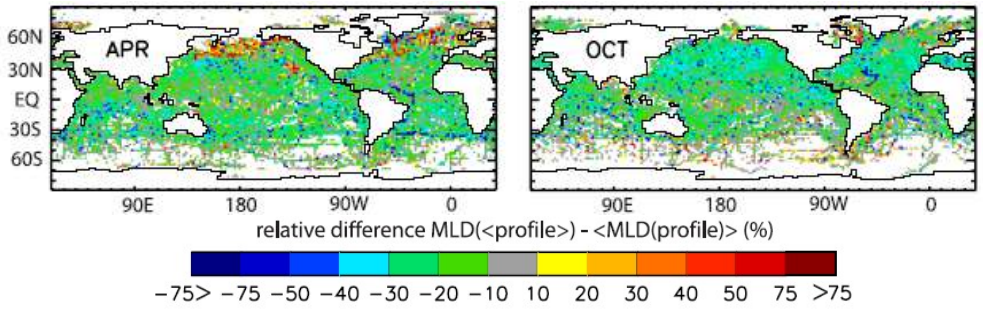

Figure 1.8 Relative difference between MLD estimated from the average profile, and average of MLDs estimated from individual profiles using ΔT = 0.2°C (de Boyer Montégut et al. 2004).

MLDs obtained from this threshold method are compared with observed ARGO climatology (Holte et al. 2017). This climatology is based on nearly 1,250,000 profiles and provides the estimates of monthly mixed layer depth and physical properties. It also provides a database of mixed layer properties, as well as the location and date, of every individual Argo profile used to assemble the climatology on global 1° × 1° gridded maps. This Argo data will be compared with MLDs estimates in this study in Chapter 2.

1.3 Stratification Index

For completeness and as an opposite concept to the MLD, the amount of ocean stratification is also an indicator of MLD variability. The stratification index (SI, [kg m^{-2}]) is a commonly used measure to assess the ocean stratification (Seyfried et al. 2017).

$$SI(Z) = \int_{Z}^{0} \big(\rho(Z) - \rho(z)\big) dz \tag{1.1}$$

where ρ is the potential density and Z is a reference level. $SI(Z) = 0$ means that the water column is well-mixed, at least to depth Z or, in other words, that the MLD is greater or equal to Z.

1.4 Energy Conversion

During mixing and stratification processes, a large amount of energy conversion between the potential and kinetic energy is expected. In order to investigate the characteristics of this energy conversion in the ocean, the so-called available potential energy and kinetic energy are used. The available potential energy is the utilizable potential energy to be converted to kinetic energy. To derive the available potential energy, the parcel theory is applied. Consider a vertical exchange of two parcels at different heights. The instantaneous potential energy (PE) can be defined as:

$$PE = MgZ_c \tag{1.2}$$

where M refers to the total mass, g is the Earth's acceleration of gravity and Z_c is the center of mass of both water masses.

The lowest potential energy ($\overline{PE}$) equilibrium state can be expressed as:

$$\overline{PE} = Mg\overline{Z_c} \tag{1.3}$$

where $\overline{Z_c}$ is the average center of mass of both water masses. The instantaneous available potential energy (APE) is defined as:

$$APE = PE - \overline{PE} = Mg(Z_c - \overline{Z_c}) \tag{1.4}$$

This APE can be simplified as:

$$APE = -\rho_0 bZ \approx \rho_0 \frac{b^2}{N^2} \tag{1.5}$$

where $N^2 = \frac{-g}{\rho_0}\frac{\partial \rho}{\partial z}$ is the squared Brunt–Väisälä frequency (unit: s^{-2}) and $b = -g\frac{\rho_0 - \rho}{\rho_0}$ is the buoyancy [m s^{-2}]; ρ_0 and ρ are the reference density and the density of the water mass.

The mean kinetic energy for a flow in geostrophic balance is defined as:

$$KE = \frac{\rho_0}{2}(u^2 + v^2) \tag{1.6}$$

where, u and v are the zonal (x direction) and meridional (y direction) velocity (m/s) respectively.

The ratio between the kinetic energy and the available potential energy can be arranged as:

$$\frac{KE}{APE} \sim \frac{N^2H^2}{f^2L^2} = \frac{N^2U^2}{B^2} \tag{1.7}$$

where, H is water depth, L is characteristic horizontal length scale, f is planetary vorticity, U is characteristic velocity, and B is buoyancy.

We note that this calculation for the APE and the KE should be considered as a first guess to track the energy conversion because it does not differentiate between the mean and the eddy energetic contributions nor takes into account the dissipated energy. For a more accurate approach the Lorenz cycle can be computed; however, it requires an almost enclosed system and a quasi-stationarity of the system, far from the Labrador Sea conditions, which receives a seasonal flow of dense water masses trough the Davis Strait and the Irminger Sea, and the Labrador Water transports a large amount of energy into the open Atlantic Ocean.

1.5 Instabilities in the Ocean

Convection, stratification and energy conversion mechanisms introduced in Sections 1.2 to 1.4 take place in forms of instabilities. These instabilities can be detected and classified by the Ertel potential vorticity and the balanced Richardson angle, and they provide the information about the formation of the instabilities. This section introduces the Ertel potential vorticity and the balanced Richardson angle and explains several instability modes by means of these measures.

1.5.1 Ertel Potential Vorticity

The existence of ocean instabilities can be determined by checking whether the Ertel potential vorticity, q, has the opposite sign of Coriolis parameter, f (Hoskins 1974), i.e.

$$fq < 0 \tag{1.8}$$

where the Coriolis parameter is $f = 2\Omega sin\phi$ and $q = \left(f\hat{k} + \nabla \times \vec{u}\right)\nabla b$ is the Ertel potential vorticity, in which $\vec{u}$ is the velocity field and b is buoyancy flux. This Ertel potential vorticity can be decomposed into the vertical (q_{vert}) and the baroclinic (q_{bc}) components:

$$q = q_{vert} + q_{bc} \tag{1.9}$$

q_{vert} is the composition of the vertical component of the absolute vorticity and the stratification:

$$q_{vert} = \zeta_{abs}N^2 \tag{1.10}$$

q_{bc} is the composition of the horizontal vorticity and the horizontal buoyancy gradient:

$$q_{bc} = \left(\frac{\partial u}{\partial z} - \frac{\partial w}{\partial x}\right)\frac{\partial b}{\partial y} + \left(\frac{\partial w}{\partial y} - \frac{\partial v}{\partial z}\right)\frac{\partial b}{\partial x} \tag{1.11}$$

Under the assumption of geostrophic balance and by applying the thermal wind relationship, the baroclinic component of the Ertel potential vorticity is simplified as:

$$q_{bc}^{g} = -f\left|\frac{\partial \vec{u}_g}{\partial z}\right|^2 = -\frac{1}{f}|\nabla_h b|^2 \tag{1.12}$$

Under stable conditions, when a water mass is perturbed it tends to oscillate around its center of gravity and, after a while, the oscillation fades and the water mass returns to its equilibrium state. In the event that this perturbation grows with time the water mass may move away, and an instability develops.

1.5.2 Balanced Richardson Number / Angle

The balanced Richardson number (Ri_B) is a quantitative criterion to determine what kind of instabilities can develop. It is defined as the ratio between the squared vertical and the horizontal buoyancy gradients weighted by the squared planetary vorticity:

$$Ri_B = \frac{N^2}{\left(\partial \vec{u}_g/\partial z\right)^2} \equiv \frac{f^2 N^2}{|\nabla_h b|^2} \tag{1.13}$$

The potential vorticity of a geostrophic flow is negative, i.e. instabilities take place, when the balanced Richardson number meets the following conditions:

$$Ri_B < \frac{f}{\zeta_g} \quad \text{if } \zeta_g f > 0 \tag{1.14}$$

where $\zeta_g = f + \nabla \times \vec{u}_g \hat{k}$ is the vertical component of absolute vorticity in geostrophic balance. The balanced Richardson number is favorable to understand principles of instability criterion, but tedious to deal with its values due to its infinite range, i.e. $-\infty < Ri_B < \infty$. Therefore, it is more convenient to use the balanced Richardson angle, which provides the same information expressed as an angle, which is more advantageous to handle because of its finite range ($-180° < \phi_{Ri_B} < 0°$).

The balanced Richardson angle is defined as:

$$\phi_{Ri_B} = \tan^{-1}\left(-\frac{1}{Ri_B}\right) = \tan^{-1}\left(-\frac{|\nabla_h b|^2}{f^2 N^2}\right) \tag{1.15}$$

and instabilities occur when

$$\phi_{Ri_B} < \phi_c \equiv \tan^{-1}\left(-\frac{\zeta_g}{f}\right) \tag{1.16}$$

1.5.3 Instability Type

The balanced Richardson number (Ri_B) is a quantitative criterion to determine what kind of instabilities can develop given some vorticity and buoyancy conditions in a region and is defined as the ratio between vertical and horizontal components. The different instabilities that can be determined from the balanced Richardson angle are now described:

a. Pure Gravitational Instability

When a spatially uniform buoyancy is present in a spatially uniform stratified ocean, purely vertical upright convection takes place when a water mass is perturbed, which is depicted in Figure 1.9 (a). This mechanism is called pure gravitational instability.

Pure gravitational instability is an extreme case and rarely happens in reality because in the ocean there are numerous inhomogeneities e.g. insolation difference, unequal wind forcing, bathymetric features, etc. that avoid an only vertical displacement of the water mass. However, under strong atmospheric cooling conditions an almost vertical instability is expected.

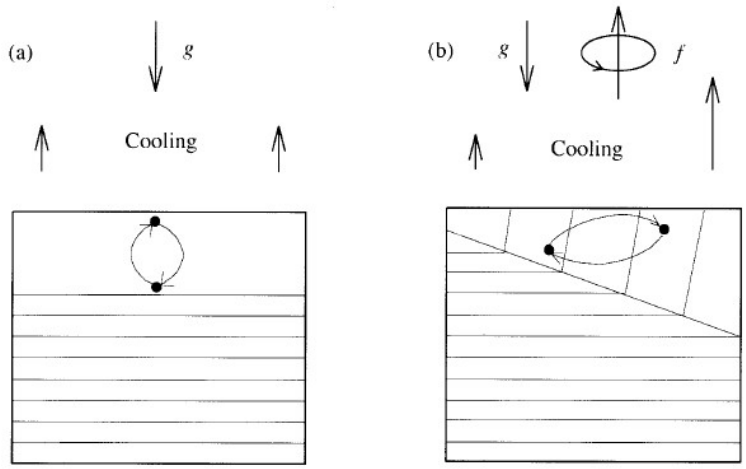

Figure 1.9 (a) Schematic of pure gravitational instability and (b) symmetric instability (adapted from Haine et al. (1998)).

b. Pure Inertial Instability

Suppose a well-mixed upper layer condition in vertical and in horizontal ($N^2 = 0$ and uniform density) and barotropic currents that only changes meridionally (y-axis). Then, all the energy is in kinetic form. In this situation if overturning occurs in the y-z plane with no variation in x, instability arises because kinetic energy is converted to potential energy. This instability is called pure inertial instability. The pure inertial instability is efficient in the horizontal direction because the barotropic current does not vary with depth. Hence, the magnitude of pure inertial instability depends on meridional velocity shear and on the planetary vorticity.

c. Gravitational/Inertial Symmetric Instability

As explained above, pure gravitational and pure inertial instabilities hardly occur due to numerous inhomogeneities in the ocean and vertical changes in the currents (e.g. induced by bottom friction). In the real ocean, because of the interaction between the currents and buoyancy fluxes, a combination of upright and lateral exchanges take place simultaneously. As a result, slantwise (diagonal) convection, i.e. a combination of pure gravitational and pure inertial instabilities occurs, which is called gravitational/symmetric instability, symmetric instability or symmetric/inertial instability depending on the vertical stability and on the buoyancy gradients.

All the above instabilities can be classified based on the Richardson angle, the dominance of the vertical (f^2N^2) or the horizontal buoyancy gradients ($|\nabla_h b|^2$). Figure 1.10 illustrates the instabilities that can develop according to the value of the balanced Richardson angle, which depends on the sign of the relative vorticity (left plot for anticyclonic relative vorticity; right plot for cyclonic relative vorticity) (Thomas et al. 2013).

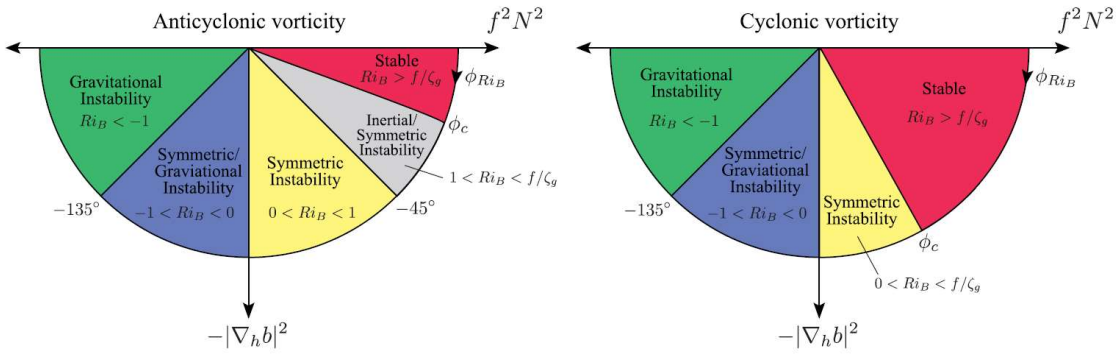

Figure 1.10 Schematic illustrating the relation between the angle ϕ_{Ri_B} to the various overturning instabilities that arise when $fq < 0$ and the vorticity is anticyclonic (left) and cyclonic (right) (Thomas et al. 2013).

Gravitational instabilities occur under an unstable stratification ($N^2 < 0$) and when the squared vertical buoyancy gradient weighted by the squared planetary vorticity dominates over the squared magnitude of the horizontal buoyancy gradient ($|f^2N^2| > |\nabla_h b|^2$) or, in terms of the Richardson angle, when $-180° < \phi_{Ri_B} < -135°$ (green section in Figure 1.10).

Symmetric/gravitational instabilities also occur under an unstable stratification ($N^2 < 0$), but in this case, the squared magnitude of the horizontal buoyancy gradient dominates over the squared vertical buoyancy gradient weighted by the squared planetary vorticity ($|\nabla_h b|^2 > |f^2N^2|$) or, in terms of the Richardson angle, $-135° < \phi_{Ri_B} < -90°$ (purple section in Figure 1.10).

The conditions for symmetric instability according to Figure 1.10 are the following. For stable stratification ($N^2 > 0$), symmetric instability can be found when $-90° < \phi_{Ri_B} < -45°$ in anticyclonic vorticity and when $-90° < \phi_{Ri_B} < \phi_c$ in cyclonic vorticity. This instability is present when the horizontal component ($|\nabla_h b|^2$) is larger than the vertical component (f^2N^2) of the Richardson angle (yellow section in Figure 1.10).

Inertial Instability takes place when $-45° < \phi_{Ri_B} < \phi_c$ and only in anticyclonic vorticity condition (gray section in Figure 1.10). This instability can develop when the vertical component (f^2N^2) is larger than the horizontal component ($|\nabla_h b|^2$) of the Richardson angle (Hoskins 1974, Haine et al. 1998).

Table 1.4 provides the summary of conditions and abbreviations for the main type of instabilities.

Type	Stratification	Richardson Balance	Richardson Angle	Note
Stable	Stable ($N^2 > 0$)	$f^2N^2 > 0$	$\phi_{Ri_B} > \phi_c$	$\phi_c \equiv \tan^{-1}\left(-\frac{\zeta_g}{f}\right)$
Pure Inertial Instability (PII)	Uniform ($N^2 = 0$)	$\lvert f^2N^2\rvert = \lvert\nabla_h b\rvert^2 = 0$	Indeterminant	
Inertial/ Symmetric Instability (ISI)	Stable ($N^2 > 0$)	$\lvert f^2N^2\rvert > \lvert\nabla_h b\rvert^2$	$-45° < \phi_{Ri_B} < \phi_c$	Only for anticyclonic relative vorticity
Symmetric Instability (SI)	Stable ($N^2 > 0$)	$\lvert f^2N^2\rvert < \lvert\nabla_h b\rvert^2$	$-90° < \phi_{Ri_B} < -45°$ $-90° < \phi_{Ri_B} < \phi_c$	For anticyclonic relative vorticity For cyclonic relative vorticity
Symmetric/ Gravitational Instability (SGI)	Unstable ($N^2 < 0$)	$\lvert f^2N^2\rvert < \lvert\nabla_h b\rvert^2$	$-135° < \phi_{Ri_B} < -90°$	
Gravitational Instability (GI)	Unstable ($N^2 < 0$)	$\lvert f^2N^2\rvert > \lvert\nabla_h b\rvert^2$	$-180° < \phi_{Ri_B} < -135°$	
Pure Gravitational Instability (PGI)	Unstable ($N^2 < 0$)	$f^2N^2 < 0$ and $\lvert\nabla_h b\rvert^2 = 0$	$\phi_{Ri_B} = -180°$	

Table 1.4 Summary of the types of instabilities according to the Richardson angle.

1.5.4 Baroclinic Instability

However, the above instabilities are not able to completely mix the ocean, thus leaving space for the development of baroclinicities from the remaining potential energy. These baroclinic instabilities can eventually result in the formation of coherent eddies of geostrophic scales (from tens to hundreds of km) that contribute to restratify the ocean. As a result, there is a permanent competition between the instabilities shown in Table 1.4 (that aid to mix the ocean) and the baroclinic instabilities (which aid to restratify the ocean) in a never ending seasonal cycle.

1.6 Objectives & Research Questions

In this study, the dataset presented in Section 1.1.2 is used to analyze the dynamics behind mixed layer seasonality in the Labrador Sea. To do this, first, an evaluation of spatial and temporal patterns of the mixed layer depth and energy conversion is made. Second, to better understand the mixed layer depth variability, dominant types of instability and the dominant baroclinic modes are determined. It is hypothesized that these instabilities drive the energy conversion and the subsequent growth of coherent mesoscale eddies, which can help to restratify the MLD in two ways: by flattening the sloping isopycnals when they form; and by lateral heat and mass exchanges between the warmer boundary and the cooler interior of the Labrador Sea. The questions addressed in this thesis are:

(1) Which is the best method to compute the mixed layer depth in the Labrador Sea?
(2) Where and when does the highest conversion between potential and kinetic energies occur?
(3) How do the absolute vorticity and the vertical and horizontal buoyancy gradients behave in the Labrador Sea? What kind of instabilities can be identified from the imbalances between the absolute vorticity and buoyancy gradients? How do they change in space and time?
(4) How do ocean eddies affect the restratification of the upper layers?
(5) How do these processes interact? What comprehensive patterns can we observe?

1.7 Approaches to Answer Research Questions

This research consists of five phases based on the above research questions, which are summarized in Figure 1.11:

(1) Spatial and temporal patterns of the mixed layer depth are investigated. To compute the MLD, the widely spread threshold method is used. Several threshold values of potential temperature and potential density are evaluated and computed and compared against observed data, and the most appropriate threshold value for the Labrador Sea is selected. (see Section 1.2 and 1.3)
(2) Spatial and temporal patterns of the energy conversion are investigated by means of APE and KE. These patterns are compared to those of the mixed layer depth. This energy conversion process is the first step to understand the mixed layer variability in the Labrador Sea. (see Section 1.4)
(3) The existence of instabilities presumably responsible for the energy exchange are identified by computing the Ertel potential vorticity. Next, instabilities are identified by computing the Richardson angle. (see Section 1.5.1 and 1.5.2)
(4) The degree of baroclinicity and the potential development of mesoscale eddies in the Labrador Sea are evaluated. It is also assessed whether the presence of eddies affects the restratification process and the reduction of the mixed layer depth. Based on previous studies, it is expected that these eddies play a key role in the spring Labrador Sea restratification. (see Section 1.5.3)
(5) To conclude, the connection among MLD variability, energy exchanges, the existence of instabilities, the growth of baroclinicities and the presence of eddies are explored and further discussed.

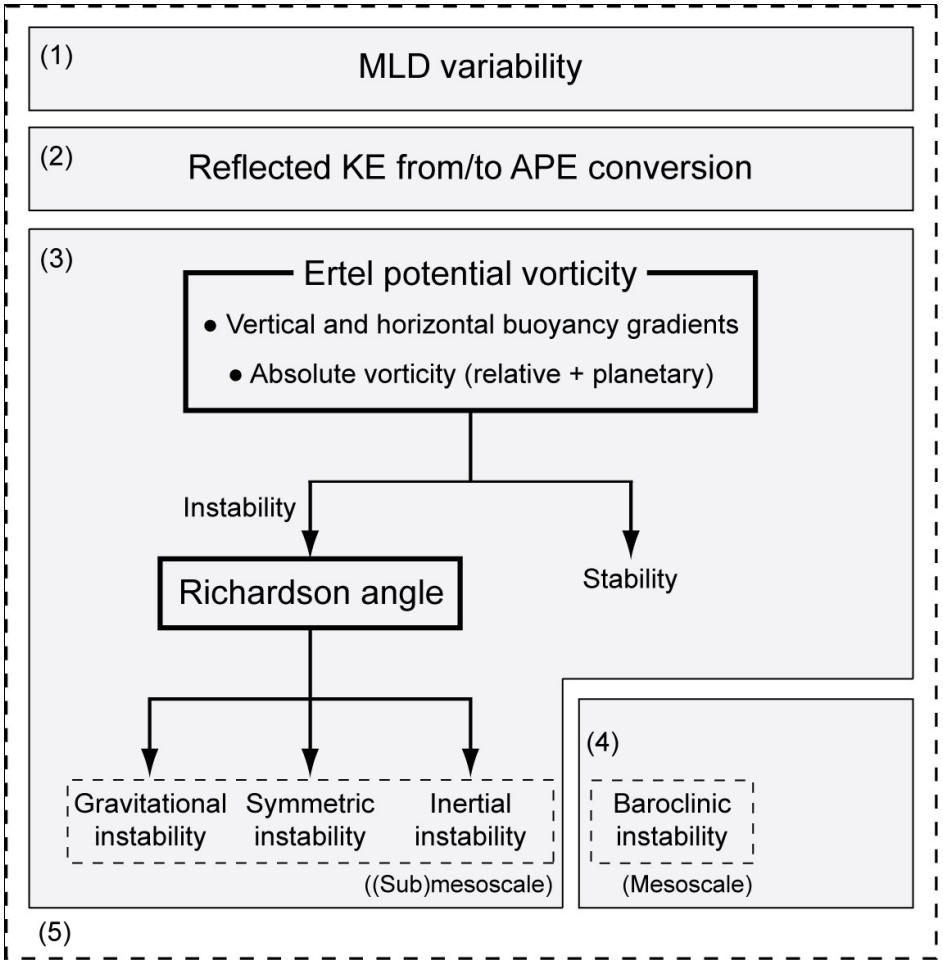

Figure 1.11 Research framework.

2. Mixed Layer Depth

This chapter discusses spatial and temporal patterns of the mixed layer depth (MLD). It aims to provide basic insight on the MLD in the Labrador Sea. MLDs are computed with the threshold method using potential temperature and potential density (Section 2.2) and later compared with those from Argo climatologies (Section 2.3). The Stratification Index is also investigated to provide another view of the MLD variability (Section 2.4). Various threshold values are evaluated and finally the most appropriate threshold value for the Labrador Sea is selected (Section 2.5).

2.1 Potential Density Computation

In order to compute density-based MLD, potential density of seawater needs to be computed first. Potential density is defined as the density that a parcel of fixed composition would acquire if moved adiabatically to a given pressure level (called reference pressure), usually taken as 1 bar (Gill 1982). This can be computed with an equation of state, and EOS-80 is used in this study (UNESCO 1981). The reference pressure is taken as 1 bar. A sketch summarizing the process is displayed in Figure 2.1.

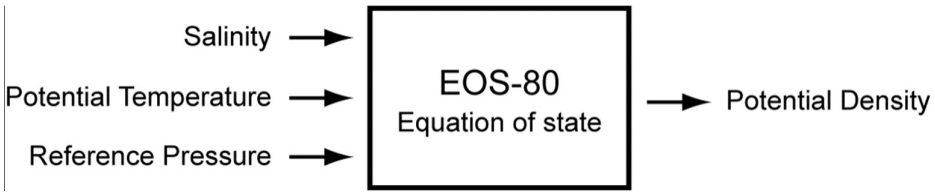

Figure 2.1 Schematization of EOS-80 inputs and output.

EOS-80 is valid for a given potential temperature within the range $0 < \theta < 40$°C, and salinity in the range $0 < S < 42$ PSU (UNESCO 1981), which is sufficient for the ranges of potential temperature and salinity in the dataset (see Figure 1.5).

2.2 Computation of MLD with the Threshold Method

As mentioned in Section 1.2, the MLD is computed with a threshold method. This method defines the MLD as the depth at which potential density or potential temperature differences from a specified reference depth exceeds a given specified threshold value (Thomson et al. 2003).

First, the reference depth was set at 10m to avoid the diurnal cycle of the surface layer (Schneider et al. 1990) and temperature variations under light winds (Price et al. 1986). Two different threshold values are used for temperature-based ($\Delta\theta = 0.2$℃ and $\Delta\theta = 0.5$℃) and density-based method ($\Delta\sigma_\theta = 0.03\ kg\ m^{-3}$ and $\Delta\sigma_\theta = 0.1\ kg\ m^{-3}$) respectively.

Figure 2.2 shows the yearly mean MLDs for each threshold method. All plots display mostly similar spatial patterns, showing the deepest MLDs in the center of the Labrador Sea (56~61°N, 46~56°W), while its neighboring region has relatively shallow MLDs. MLDs derived from larger threshold values ($\Delta\theta = 0.5$℃ and

$\Delta\sigma_\theta = 0.1\ kg\ m^{-3}$) yield deep MLDs over 1000m, while smaller threshold values ($\Delta\theta = 0.2$℃ and $\Delta\sigma_\theta = 0.03\ kg\ m^{-3}$) produce much shallower MLDs (under 800m).

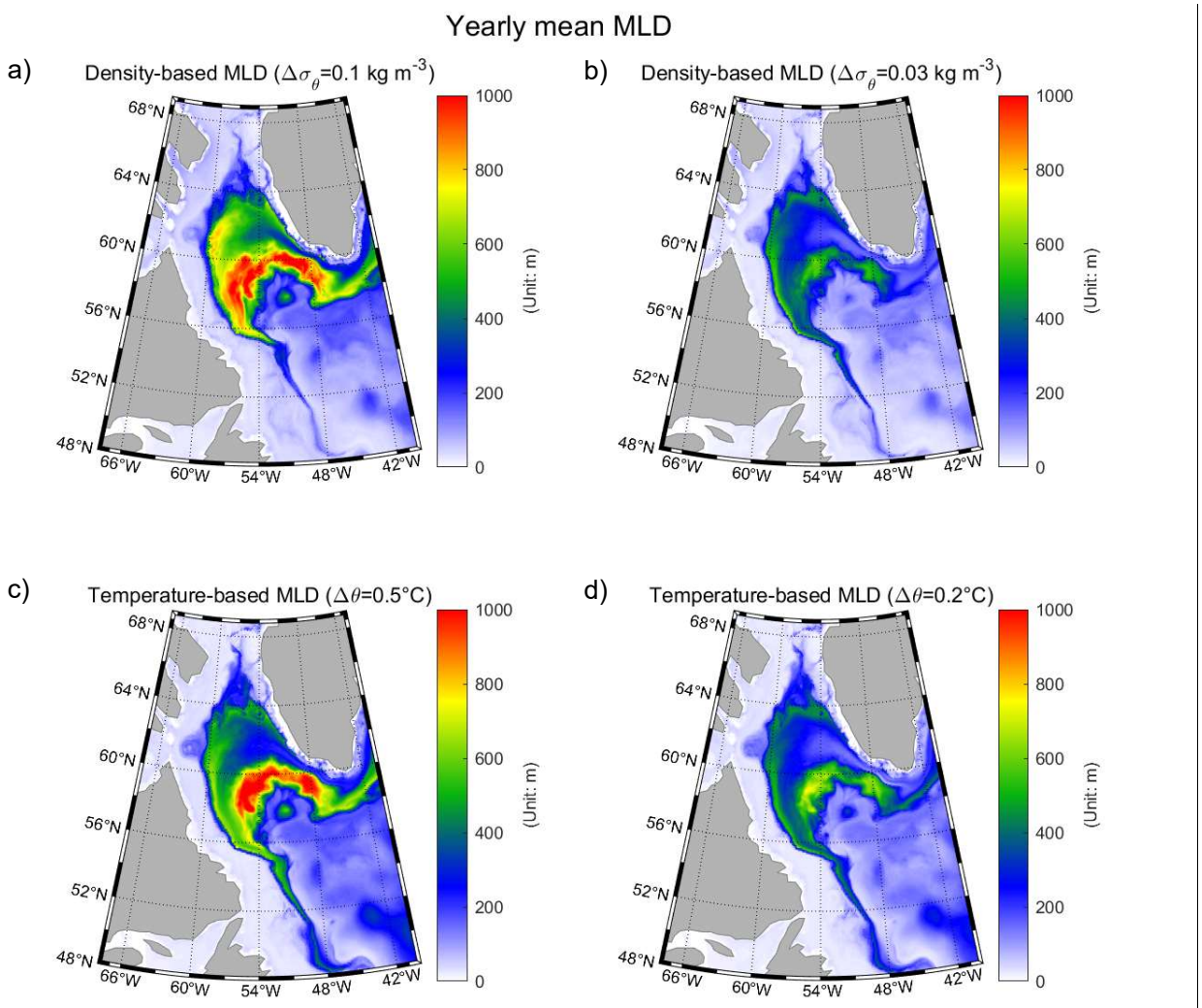

Figure 2.2 Yearly mean MLD obtained from (a) density-based threshold method with $\Delta\sigma_\theta = 0.1\ kg\ m^{-3}$, (b) $\Delta\sigma_\theta = 0.03\ kg\ m^{-3}$, (c) temperature-based threshold method with $\Delta\theta = 0.2$℃ and (d) $\Delta\theta = 0.5$℃.

Figure 2.3 presents the yearly median MLDs. Median plots shows shallower MLDs than mean plots. This result is consistent with the previous study of de Boyer Montégut et al. (2004), indicating that the mean of the MLDs often tend to be skewed to higher values (see Figures 2.2 and 2.3). Moreover, median MLDs produce different spatial patterns than mean MLDs. The MLDs in the center of the Labrador Sea are relatively shallow, while at its neighboring region, where the West Greenland and the Labrador Currents are present, the MLDs are deeper. This difference between spatial patterns of mean and median MLDs probably implies that the center of the Labrador Sea is characterized by a smoother behavior with slower changes in time (blue shading), while its surroundings display abrupt variations in time (red shading).

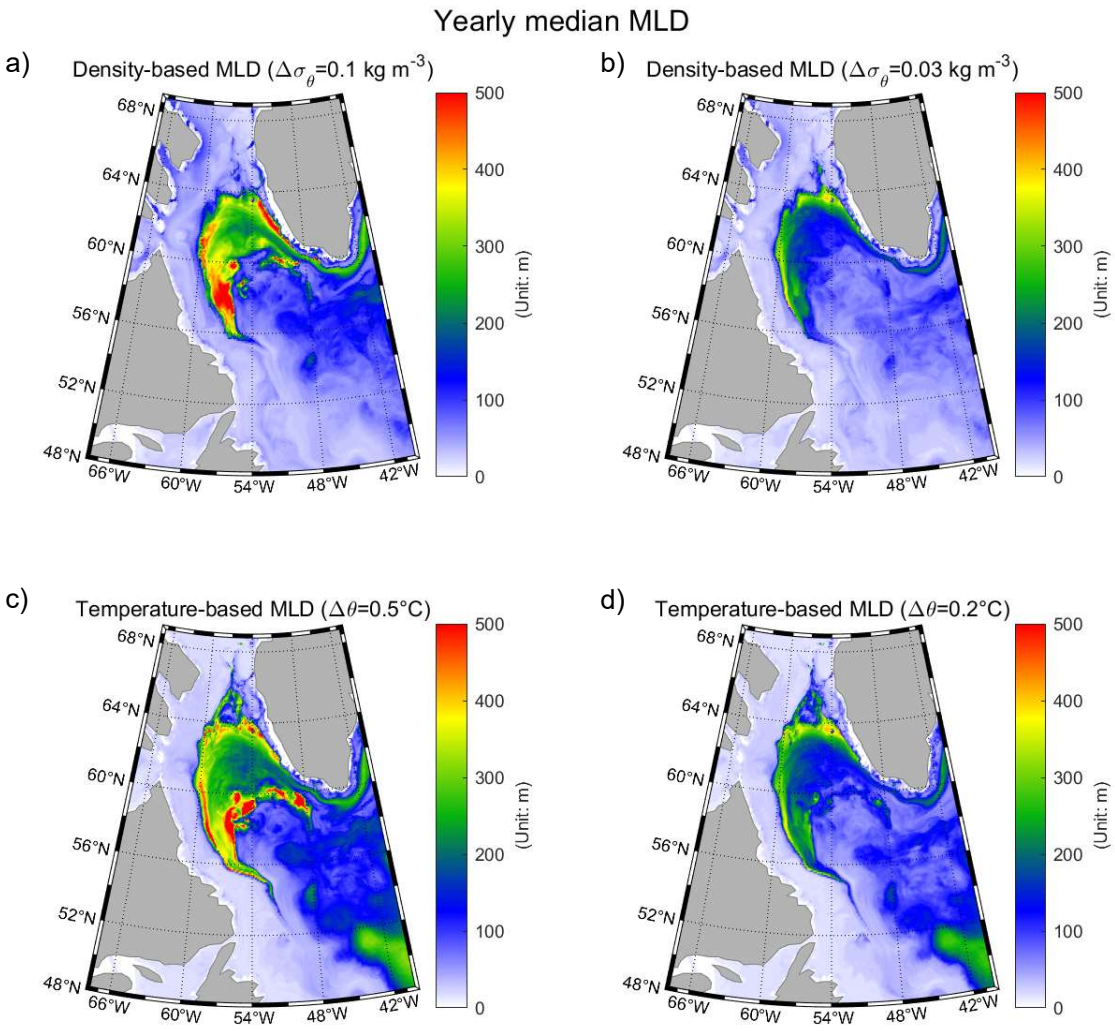

Figure 2.3 Yearly median MLD obtained from (a) density-based threshold method with $\Delta\sigma_\theta = 0.1\ kg\ m^{-3}$, (b) $\Delta\sigma_\theta = 0.03\ kg\ m^{-3}$, (c) temperature-based threshold method with $\Delta\theta = 0.2$℃ and (d) $\Delta\theta = 0.5$℃.

Figure 2.4 shows the time series of MLDs ($\Delta\sigma_\theta = 0.1\ \mathrm{kg\,m^{-3}}$, $\Delta\sigma_\theta = 0.03\ \mathrm{kg\,m^{-3}}$, $\Delta\theta = 0.5$℃ and $\Delta\theta = 0.2$℃) for three locations which have deep (55.33°W, 59.08°N, Location 1), intermediate (55.00°W, 56.75°N, Location 2), and shallow (54.08°W, 61.75°N, Location 3) MLDs respectively. Water depths are depicted with dash-dotted lines. Time series distinctly present strong seasonality (high values in winter and low values in summer), and they show large daily fluctuations that can reach thousands of meters for the most extreme cases.

The MLDs computed with a larger threshold ($\Delta\sigma_\theta = 0.1\ \mathrm{kg\,m^{-3}}$ and $\Delta\theta = 0.5$℃) are larger, even at some points MLDs are as deep as almost the whole column of water depth and reaching the bottom. And the larger threshold often provides very abrupt deepening temporal patterns (see spiky lines around April in Point 2). This sharp peaks cannot be explained by the atmospheric forcing as it changes smoothly from month to month. To limit this issue we have selected the smaller threshold as it provides more reasonable results.

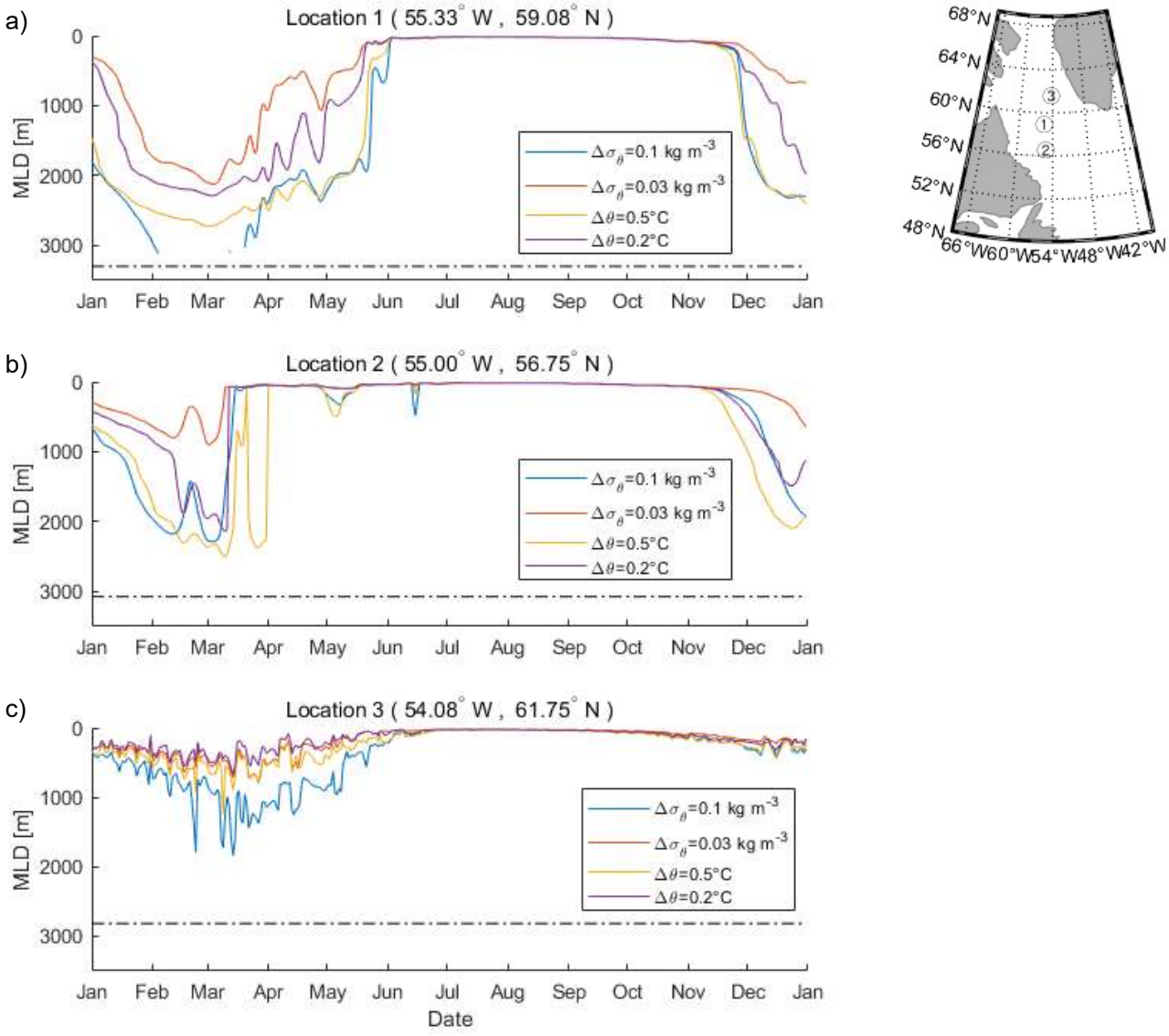

Figure 2.4 MLD time series computed with the threshold methods for three Labrador Sea locations (see inset figure) which have (a) deep (Location 1); (b) intermediate (Location 2); and (c) shallow (Location 3) MLDs respectively. Dash-dotted lines represent water deph for each location.

2.3 Comparison with Argo Climatologies

In order to evaluate the MLDs derived from model data in this study, a comparision is performed against the Argo-based gridded climatology from Holte et al. (2017). This product provides MLDs derived from Argo floats measurements interpolated onto a mesh of 2° × 2° grids. Figure 2.5 shows the yearly mean MLDs from this model data and Argo climatology. Spatial patterns of the MLDs are relatively similar for both datasets, e.g. deeper MLDs in the center of the Labrador Sea, and shallower in the surroundings. However, model data produces relatively deeper MLDs than Argo climatologies. Figure 2.6 shows the yearly median MLDs from this study and Argo climatology. Model data yields deeper MLDs than Argo data, which is in agreement with other model results (Courtois et al. 2017, Holte et al. 2017) and partly attributed to the lower spatial resolution of the gridded product and insufficient spatial coverage of Argo data.

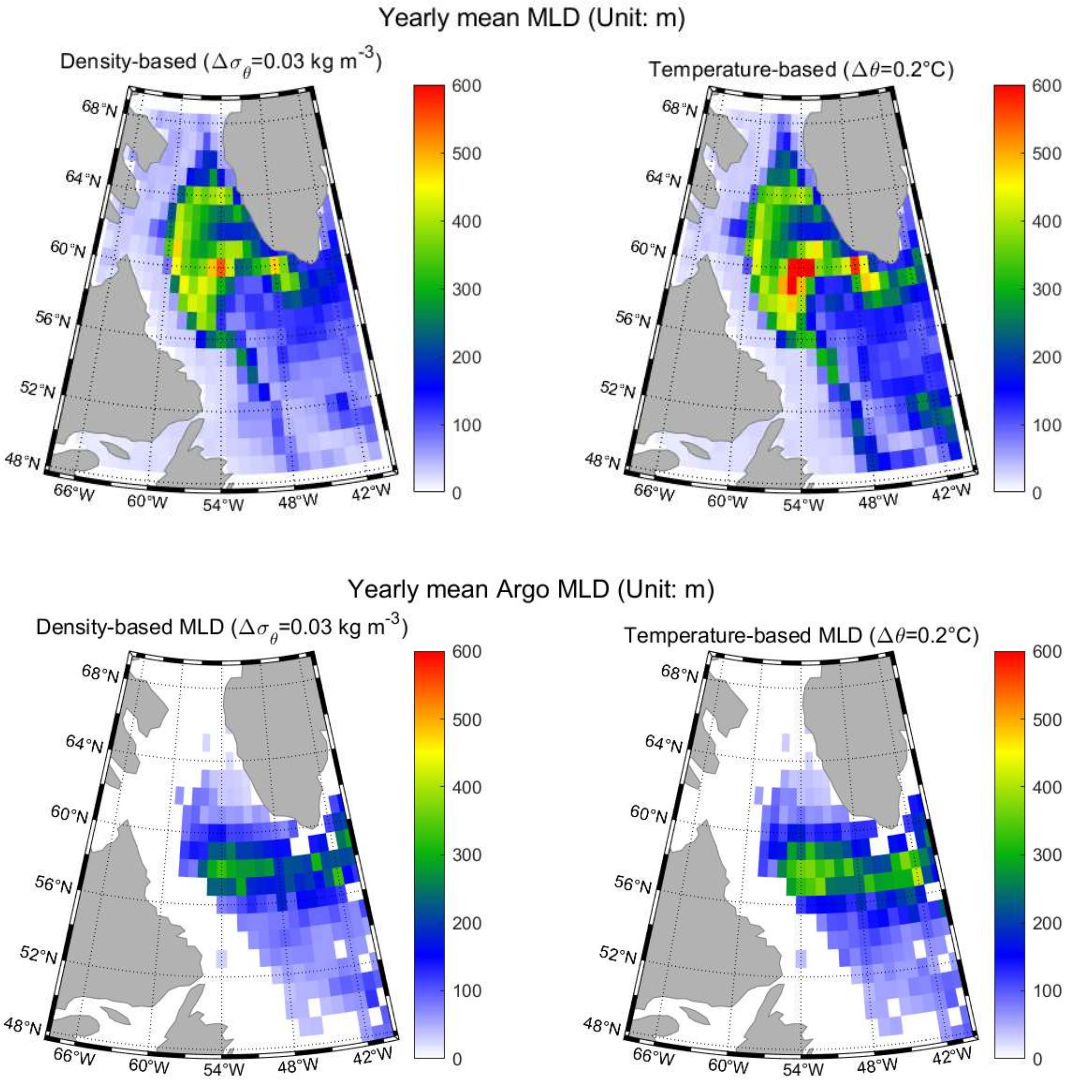

Figure 2.5 Yearly mean MLDs computed with threshold method from this study and Argo climatology.

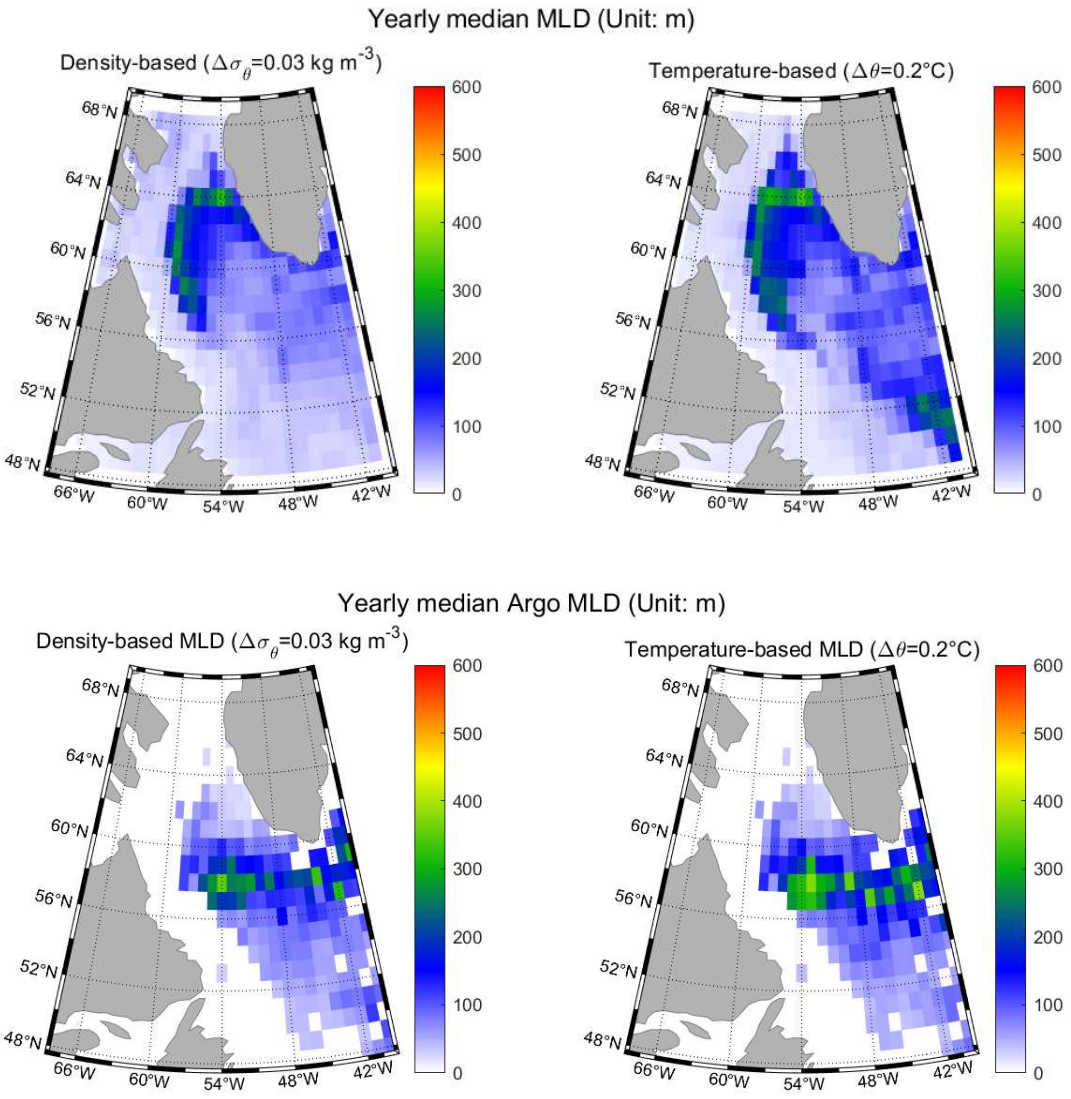

Figure 2.6 Yearly median MLDs computed with threshold method from this study and Argo climatology.

2.4 Stratification Index

Another view of the MLD variability is provided by the Stratification Index (SI), which yields a small value for well-mixed layers and a larger value for stratified layers (Section 1.3). Figure 2.7 shows the annual mean SI for reference depths of 500, 1000, 1500 and 2000m. Spatial patterns of SI for the Labrador Sea inversely correspond to those of yearly averaged MLDs.

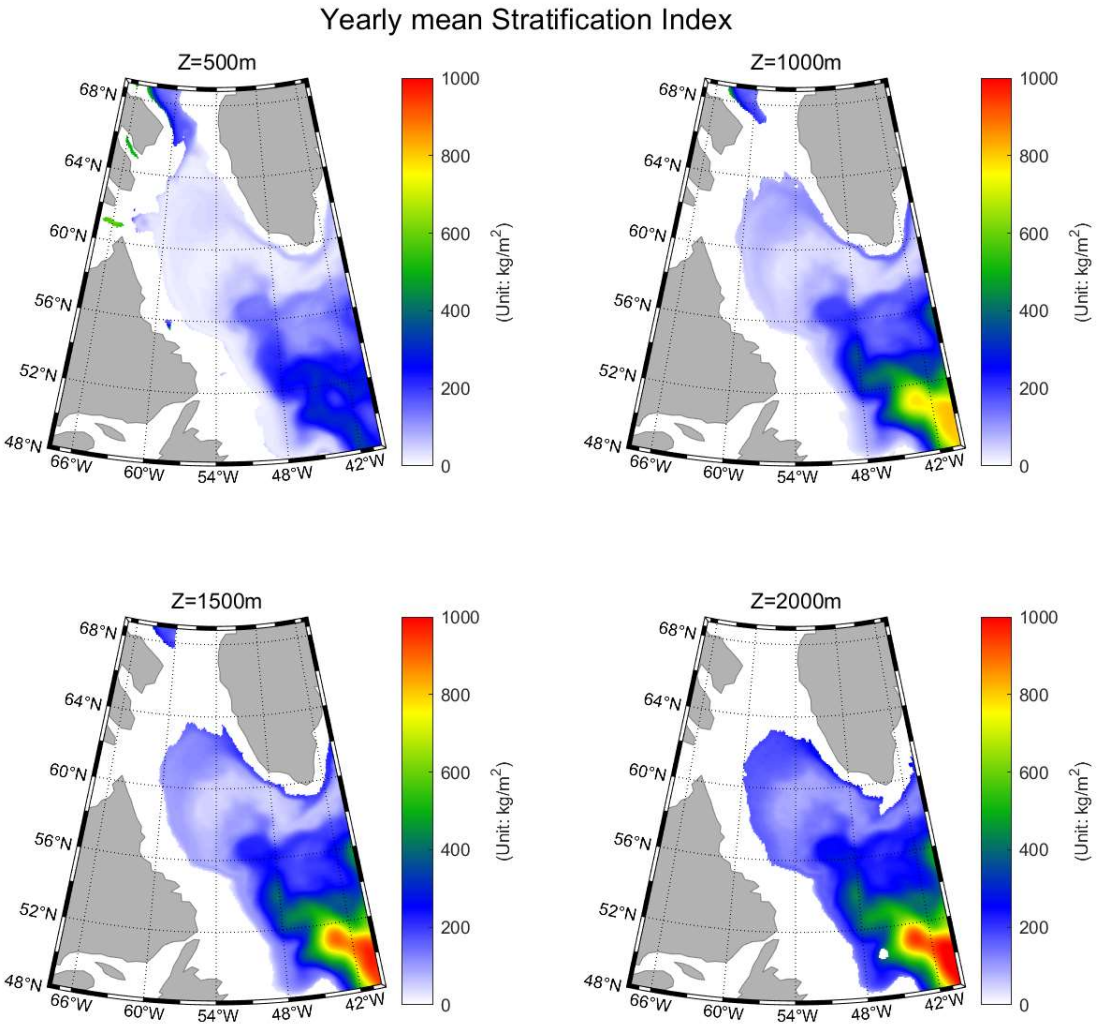

Figure 2.7 Yearly averaged Stratification Index for different reference depths (500, 1000, 1500 and 2000m respectively) in the Labrador Sea.

Time series of SI (reference depth of 500m) for three locations which have deep (55.33°W, 59.08°N, Location 1), intermediate (55.00°W, 56.75°N, Location 2), and shallow (54.08°W, 61.75°N, Location 3) MLDs respectively are plotted in Figure 2.8. The SI depicts a strong seasonality with lower values in winter and higher values in summer, which is exactly the inverse with respect to the MLD temporal patterns shown in Section 2.2.

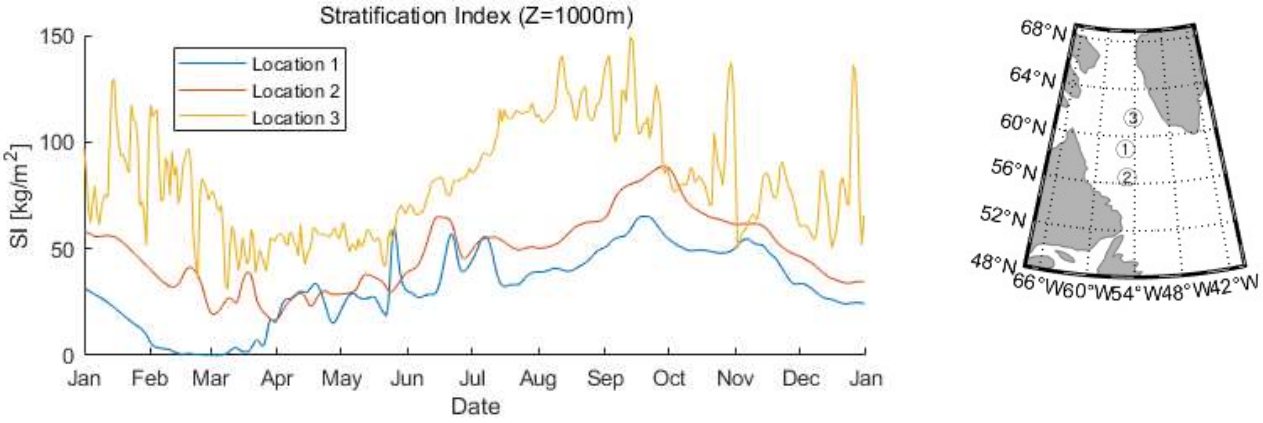

Figure 2.8 Stratification index (reference depth = 1000m) time series for three Labrador Sea locations (see inset figure) which have deep (Location 1), intermediate (Location 2), and shallow (Location 3) MLDs respectively.

2.5 Summary

To summarize the main results of this chapter, smaller potential temperature and potential density thresholds ($\Delta\theta = 0.2$℃ and $\Delta\sigma_\theta = 0.03\ kg\ m^{-3}$) provide smoother and more reasonable MLDs than the larger threshold values. Indeed, the larger thresholds yield too deep MLDs and remarkably abrupt changes at daily scales. On the other hand, density-based MLDs have a stronger physical meaning because convection and mixing processes can also be driven by salinity differences, not only by temperature. However, potential temperature-based MLDs are a complementary metric and a valid alternative when density data are not available. To conclude, it has been shown that the median is a more appropriate statistical estimator of MLDs since the mean value is often skewed to deeper values (de Boyer Montégut et al. 2004).

3. Energy Conversion

It is hypothesized that the seasonal MLD deepening and shallowing described in Chapter 2 responds to energy exchanges. In this chapter, spatial and temporal patterns of available potential energy and kinetic energy (APE and KE respectively) are discussed and connected with MLD variations.

3.1 Computation of Energy Conversion

Following Section 1.4, APE and KE can be approximated at first order with the following expressions:

$$APE \approx \rho_0 \frac{b^2}{N^2} \tag{3.1}$$

where $N^2 = \frac{-g}{\rho_0}\frac{\partial \rho}{\partial z}$ is the squared Brunt–Väisälä frequency (unit: s^{-2}) and $b = -g\frac{\rho_0 - \rho}{\rho_0}$ is the buoyancy [m s^{-2}]. ρ_0 and ρ are the reference and water mass densities respectively. In this computation, ρ_0 is set at 1000 kg/m^3.

$$KE = \frac{\rho_0}{2}(u^2 + v^2) \tag{3.2}$$

where, u and v are the zonal (x direction) and meridional (y direction) velocity (m/s) respectively.

Figure 3.1 shows the yearly mean APE and KE at a depth of 15m.

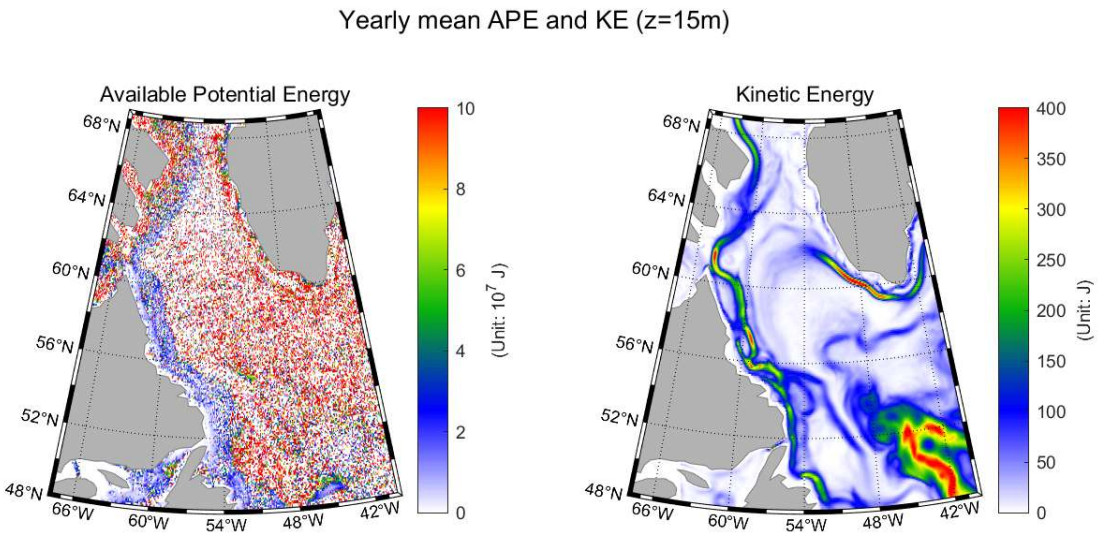

Figure 3.1 Yearly mean available potential energy and kinetic energy (z=15m, plan view)

Although the APE plot contains a lot of noise, spatial patterns of APE are well-defined; deeper locations (below 2000m) display higher APE (red color) and shallower locations (less than 500m) give lower values. KE gives less noisy patterns; high KE is observed where strong currents exist e.g. West Greenland Current (along the southwest part of Greenland) and Labrador Currents (around the Labrador continental shelves).

3.1.1 Brunt–Väisälä Frequency Computation

In order to compute the APE, the Brunt–Väisälä Frequency is needed which involves vertical differentiation. Vertical differentiation requires special care in a discrete vertical domain because it has unevenly distributed layers. Chelton et al. (1998) reviewed four different methods to estimate Brunt–Väisälä frequency, and among them, the centered potential density approach is taken because their applicability and data availability are most suitable for our study. This approach is expressed as:

$$N^2(z_{k+1/2}) = -\frac{g}{\rho_0}\left[\frac{\rho_\theta(z_k) - \rho_\theta(z_{k+1})}{z_k - z_{k+1}}\right] \tag{3.3}$$

where ρ_θ is the potential density, z_k and z_{k+1} are the standard depths, and $z_{k+1/2}$ is the midpoint between z_k and z_{k+1}.

The main reasons to choose this method are: (1) our dataset can directly be used because it requires potential density rather than normal density in the computation; and (2) the computed Brunt–Väisälä frequency is imposed on the midpoint between standard depths, which provides a more accurate computation (Chelton et al. 1998).

3.2 Spatial Patterns of Energy Conversion

One of the main difficulties in analyzing the energy conversion based on the rough approach here applied is that APE and KE have a very different order of magnitude (APE $\approx O(10^7)$ J and KE $\approx O(10^2)$ J, see Figure 3.1). In order to overcome this problem, ER is defined as the logarithm of the ratio between the integrated APE and KE, which can be expressed as below. When the ER changes, it is a sign of the energy conversion.

$$ER = log_{10}\frac{\int APE\ dz}{\int KE\ dz} \tag{3.4}$$

According to the basic theory of ocean convection, it is expected that the characteristics of energy conversion over the whole water depth and within the MLD are considerably distinct. This study defines ERs for the whole depth and for only the MLD (Eq 3.5 and 3.6) and investigates the differences between these ERs.

$$ER_H = log_{10}\frac{\int_{-H}^{0} APE\ dz}{\int_{-H}^{0} KE\ dz} \tag{3.5}$$

$$ER_{MLD} = log_{10}\frac{\int_{-MLD}^{0} APE\ dz}{\int_{-MLD}^{0} KE\ dz} \tag{3.6}$$

Figures 3.2 and 3.3 present the monthly mean ER_H and ER_{MLD} respectively. The most interesting finding from both figures is that the spatial patterns of ERs are similar to those of yearly MLD (Figures 2.2 and 2.3), especially in the center of the Labrador Sea where the deepest MLD is observed and in the southwest part

of Greenland where West Greenland Current flows. This is an expected result because mixing is generated during the conversion from potential to kinetic energy.

ER_H is roughly constant over the year, while temporal patterns or a seasonality of ER_{MLD} are evident from Figure 3.3 (considerably low values in summer season). This can be interpreted as that because a large amount of APE within the ML is released by vigorous mixing during wintertime, and the remaining APE is very little within the ML in summer season.

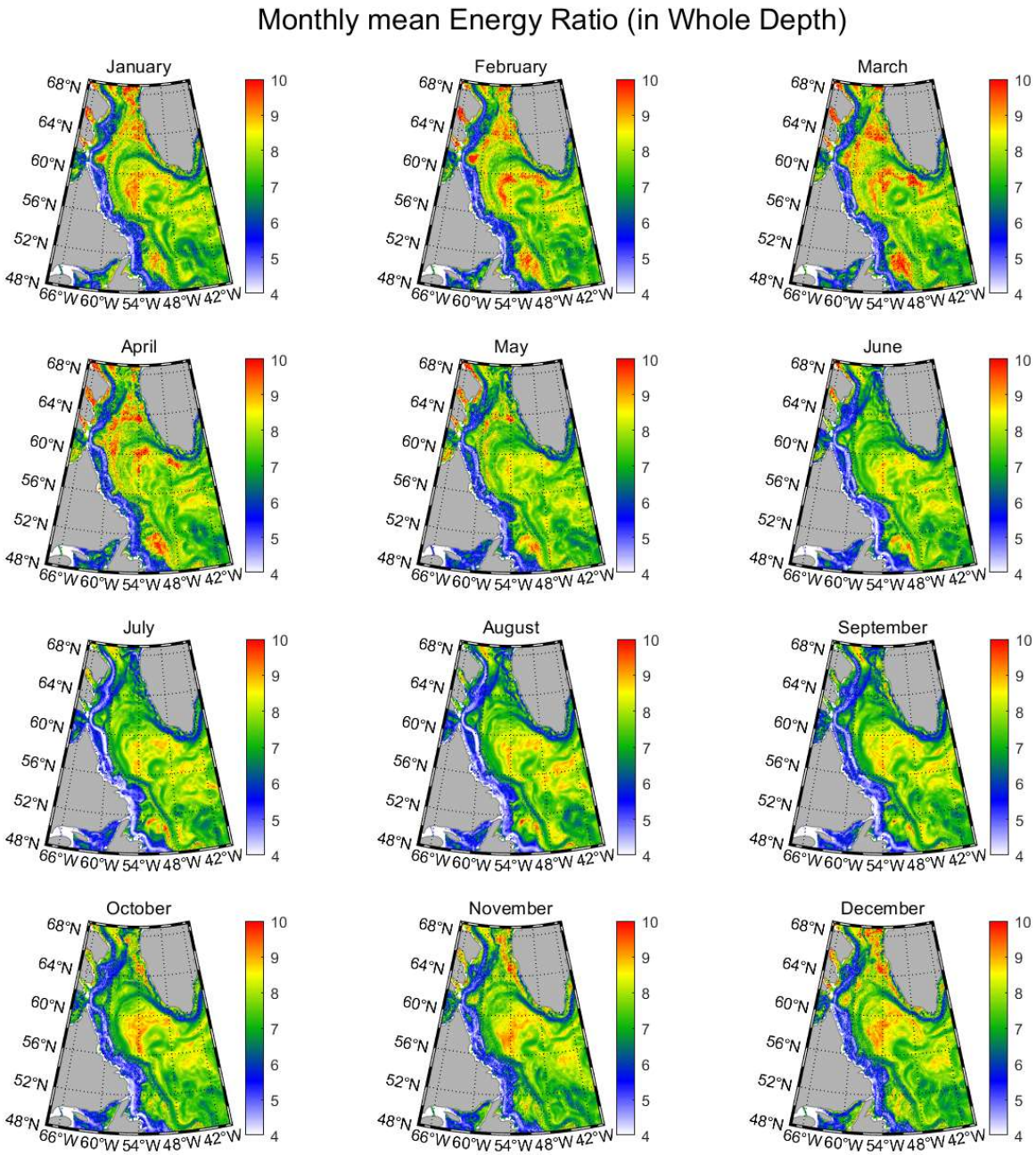

Figure 3.2 Monthly mean energy ratio over the whole depth.

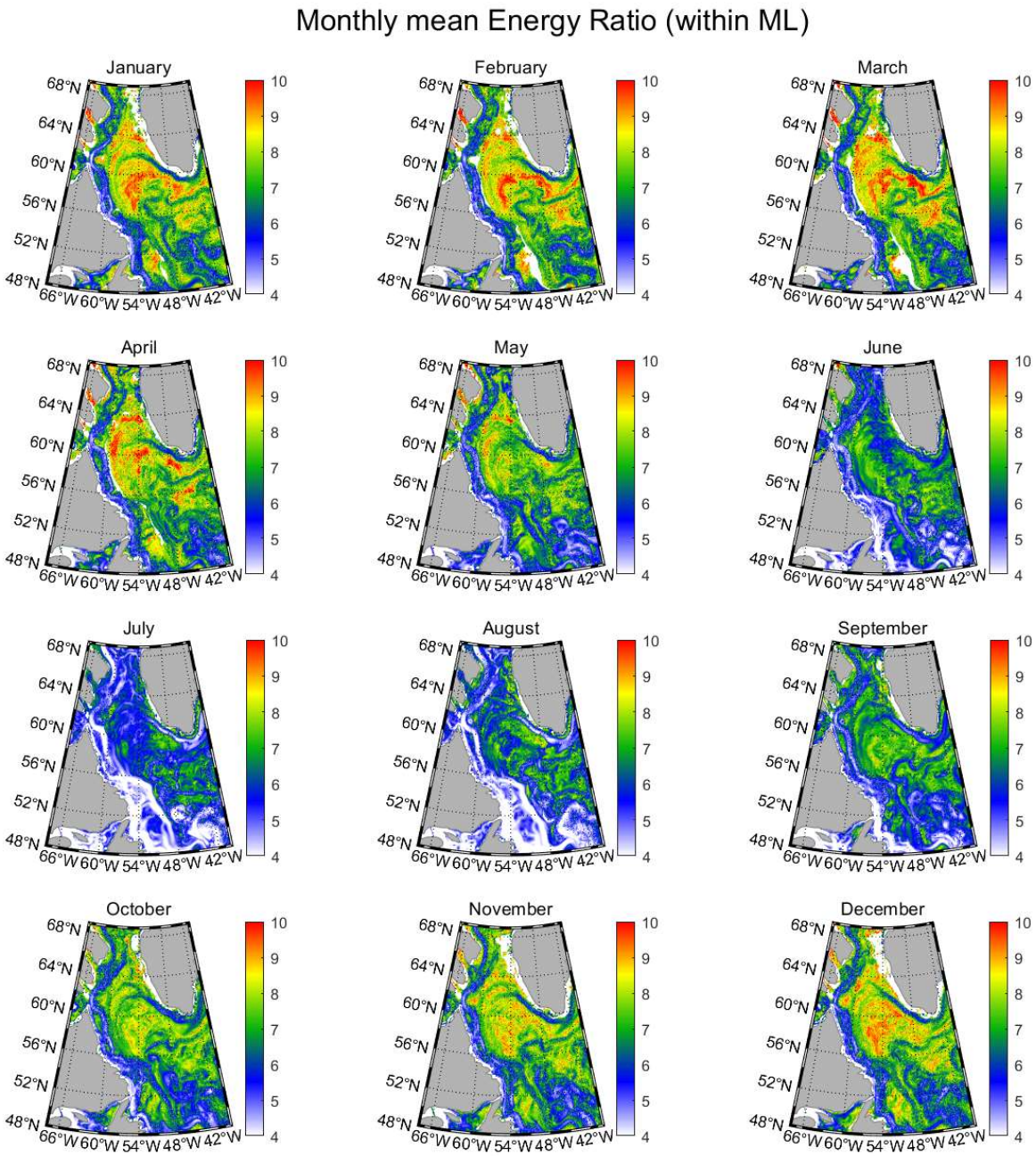

Figure 3.3 Monthly mean energy ratio within ML.

3.3 Temporal Variability of Energy Conversion

In order to investigate the temporal variability of the ER in more detail, time series of daily ERs are depicted for three locations (indicated by letters in the right panel of Figure 3.4). The selected locations correspond to where (a) the deep MLD is found (54.67°W, 59.83°N) (b) high eddy kinetic energy is found (53.75°W, 62.08°N) and (c) high eddy activity determined by the Okubo-Weiss parameter (48°W, 60°N). The basin-averaged ER time series is also given in the figure (panel d). Details regarding the formation and presence of mesoscale eddies are included in Chapter 6.

Based on results from Figure 3.4, several features can be explained. ER_H is relatively constant over the year, while ER_{MLD} displays a seasonality that lower values in summer. During wintertime ER_H and ER_{MLD} generate almost same values, but during summer ER_{MLD} deviates from ER_H. This feature is also found in the basin-averaged time series plot as well (see Figure 3.4d). This is probably because a large amount of APE is released within the ML by vigorous mixing in wintertime, and a small amount of remaining APE is present within the ML in summertime.

The temporal variation of ER between consecutive days gives a better idea of the daily energy conversion. At the location (a), large temporal changes are observed during winter, while variations are rather small during summer. From the latter, it can be inferred that a more vigorous energy conversion occurs in winter than in summer. At locations (b) and (c), time series of ER have more wiggles, and deviations of ER_{MLD} from ER_H are larger than at location (a) due to a higher KE, which is likely induced by the presence of eddies, as it is shown in Chapter 6.

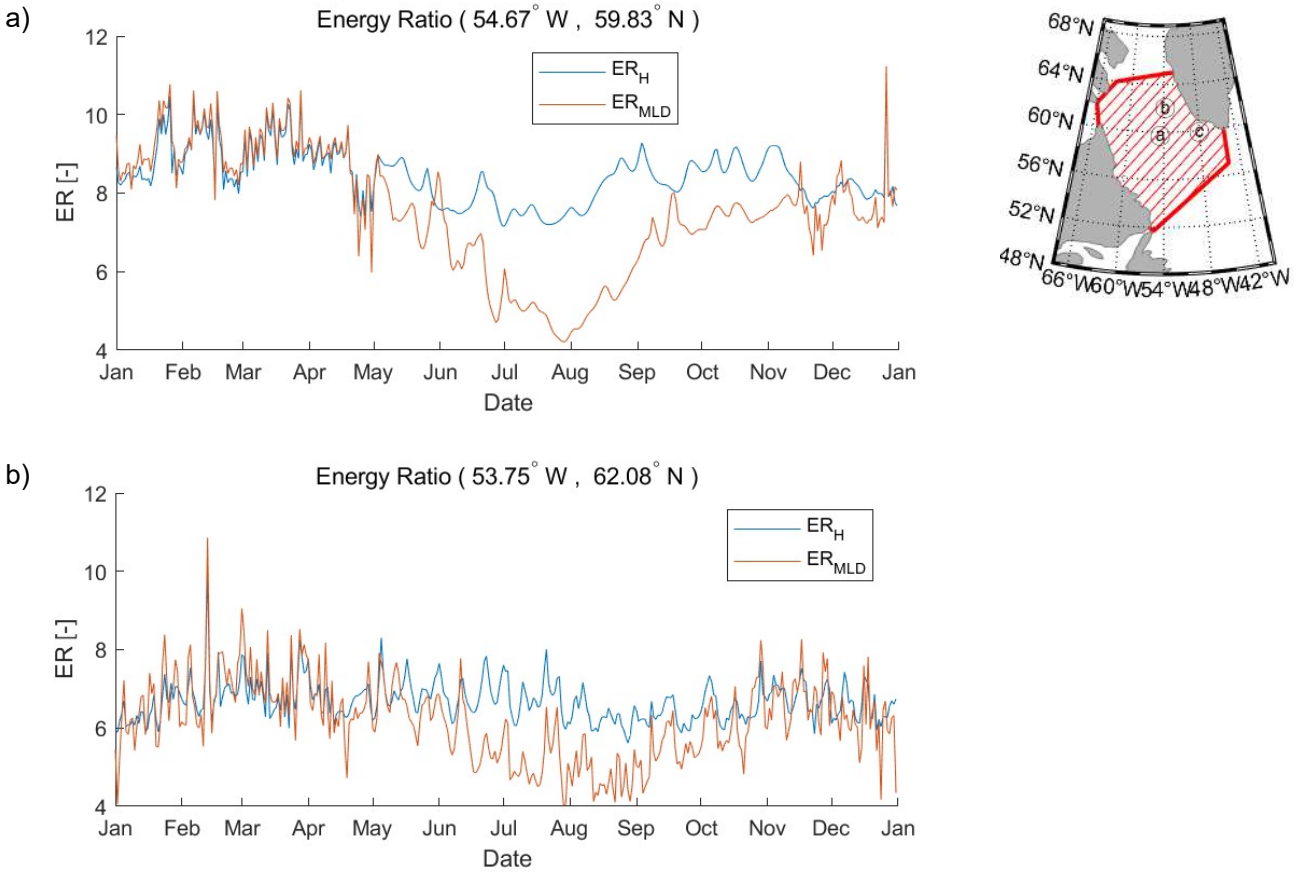

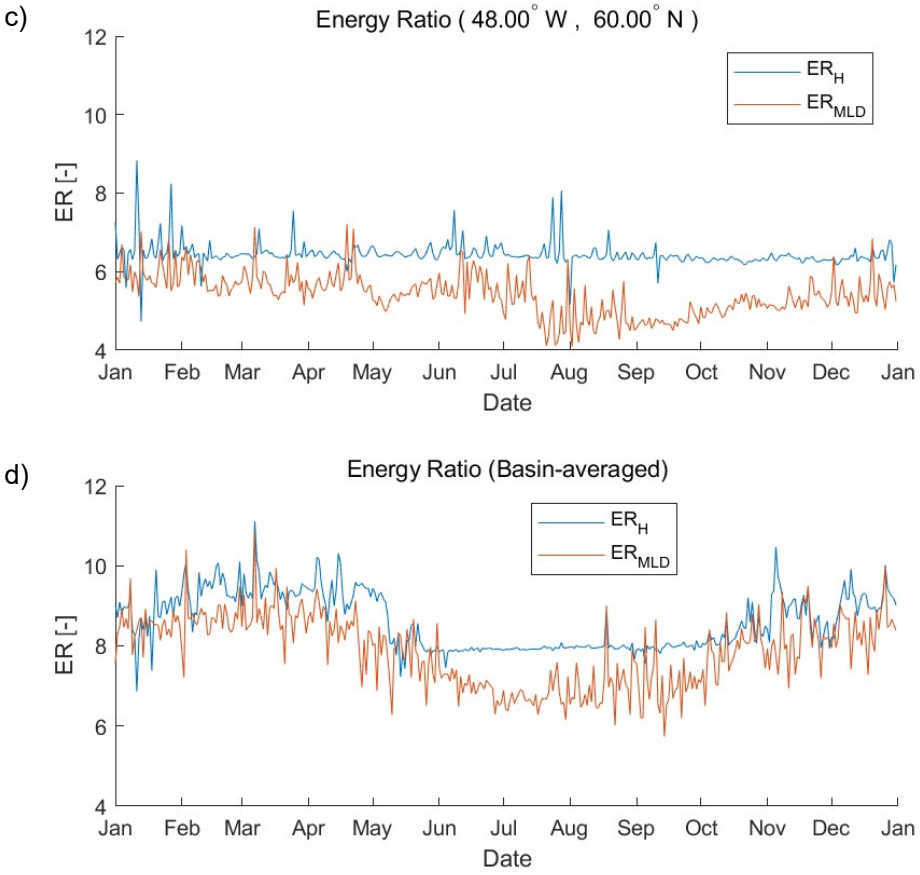

Figure 3.4 Time series of daily energy ratio (ER) for the locations (see inset figure) within the Labrador Sea where: (a) the deepest MLD is found; (b) the maximum eddy kinetic energy is found; (c) strong eddies are present; and (d) for the whole basin.

4. (Sub)mesoscale Instabilities

The previously described energy conversion must be reflected dynamically in terms of the main forces, in this case the vertical and horizontal buoyancy gradients, and in terms of the absolute vorticity. An imbalance among the above forces may result in the formation of instabilities. In this chapter, the existence of instabilities is analyzed through the Ertel potential vorticity (Section 4.1). Later, instabilities are classified by means of the Richardson angle (Section 4.2). Finally, found instabilities are quantified and further discussed in the Labrador Sea in Section 4.3.

4.1 Ertel Potential Vorticity

The Ertel potential vorticity is computed with the POP model data. As mentioned in Section 1.5.1, instabilities exist when the Ertel PV has negative values because the study region is located in the Northern Hemisphere i.e. the planetary vorticity is always positive in the location. In this computation, ρ_0 is set as 1000 kg/m^3.

Figure 4.1 shows the monthly mean Ertel PV in a plan view at a depth of 15m, and Figure 4.2 shows the same variables in a longitudinal view at 60°N. They present a clear seasonal cycle in the Ertel PV in which a lot of negative values (unstable) can be found during winter season (October – March), while the domain is full of positive values (stable) during summer season (April – September).

Another interesting feature is that almost all instabilities occur within ML, especially near the water surface (see Figure 4.2). This is expected as mixing processes are mainly driven by air–sea exchanges such as the strong cooling induced by the atmosphere.

Some instabilities are found near the bottom (not shown). This is likely due to the shear stress generated by bottom friction, which may intensify under a significant bathymetric slope as it occurs at the southern side of Greenland. However, there are some difficulties to investigate details of these instabilities because (1) the boundary layer is typically of the order of meters to tens of meters (Trowbridge et al. 2018) which is much thinner than our vertical grid size (250m) and (2) these instabilities hardly reach intermediate water depth and do not affect the upper ocean mixing process.

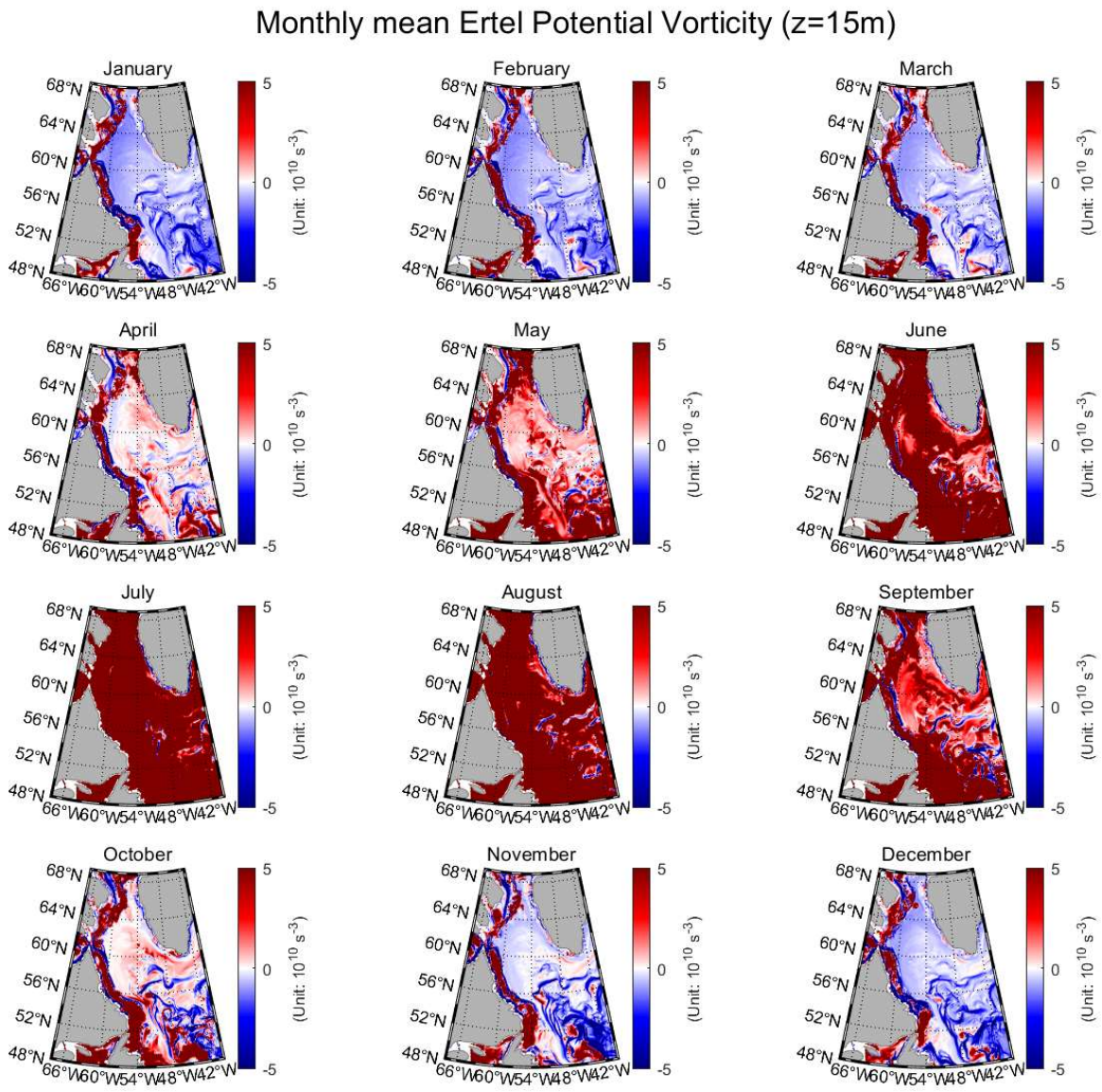

Figure 4.1 Monthly mean Ertel potential vorticity (z=15m, plan view).

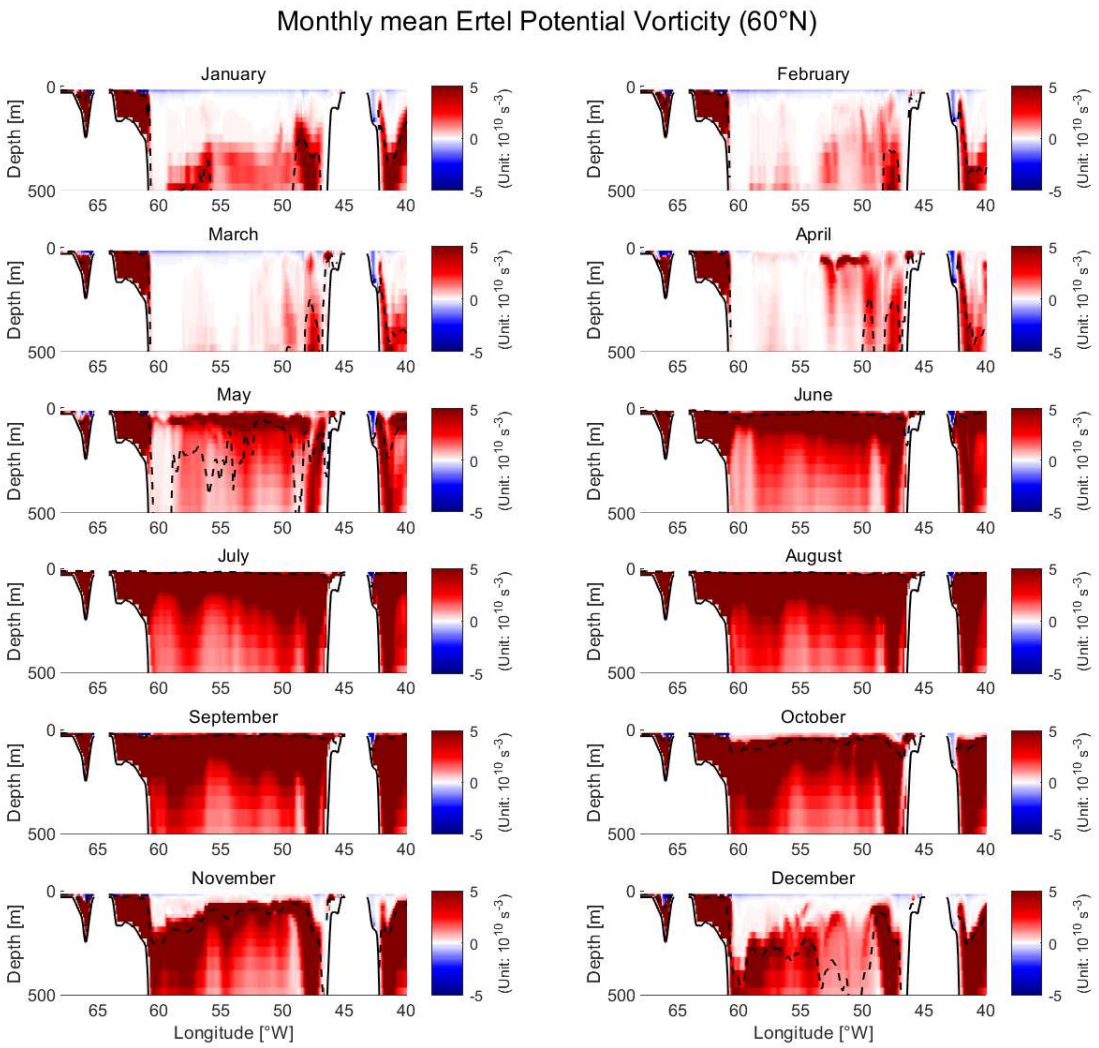

Figure 4.2 Monthly mean Ertel potential vorticity near the surface (down to 500m, 60°N, longitudinal view). The MLDs are depicted by dashed lines in the plots.

4.2 Balanced Richardson angle

The balanced Richardson angle is computed from our model data (see also Section 1.5.2). Figure 4.3 shows the monthly mean Richardson angle in a plan view at a depth of 15m, and Figure 4.4 shows the same values in a longitudinal view at 60°N. The computed values are widely ranged from -180° and 0° and they show a clear seasonal variability, in excellent agreement with MLD and Ertel PV patterns (lower values in winter indicating the formation of many instabilities, the opposite in summer). Details regarding the type of instability are investigated in Section 4.3.

During wintertime (October – March), the Baffin Bay (north from the Labrador Sea) and part of Labrador Sea have nearly -180°, and the Labrador basin gives values around -90°. In contrast, during summertime (April – September), most domain except the continental shelf in front of the Baffin Island and Newfoundland Sea (Newfoundland region of the North Atlantic, refer to Figure 1.1) reaches nearly 0°. The continental shelf in front of Baffin Island and Newfoundland Sea have around -45° in summertime.

One interesting feature is that the temporal variability in the Baffin Bay and part of the Labrador Sea is very broad (-180° in winter and 0° in summer), while in the remainder it shows a relatively narrow range (between -135° and -45°). This is probably because the Baffin Bay and part of Labrador Sea are strongly affected and unstably stratified by strong cooling in contact with the atmosphere during winter or the unstably stratified water transported into this region. A broader range in the Richardson angle means that the region is more affected by the vertical buoyancy gradients (f^2N^2) than by the horizontal ones ($|\nabla_h b|^2$) (see 1.5.3.c).

A cross-section of the monthly mean Richardson angle at 60°, shows that it is almost -180° near the surface and it rapidly increases at water depth between 100m and 200m (Figure 4.4). Between 200m and 300m the ocean presents almost 0°, which corresponds to a predominant stable state.

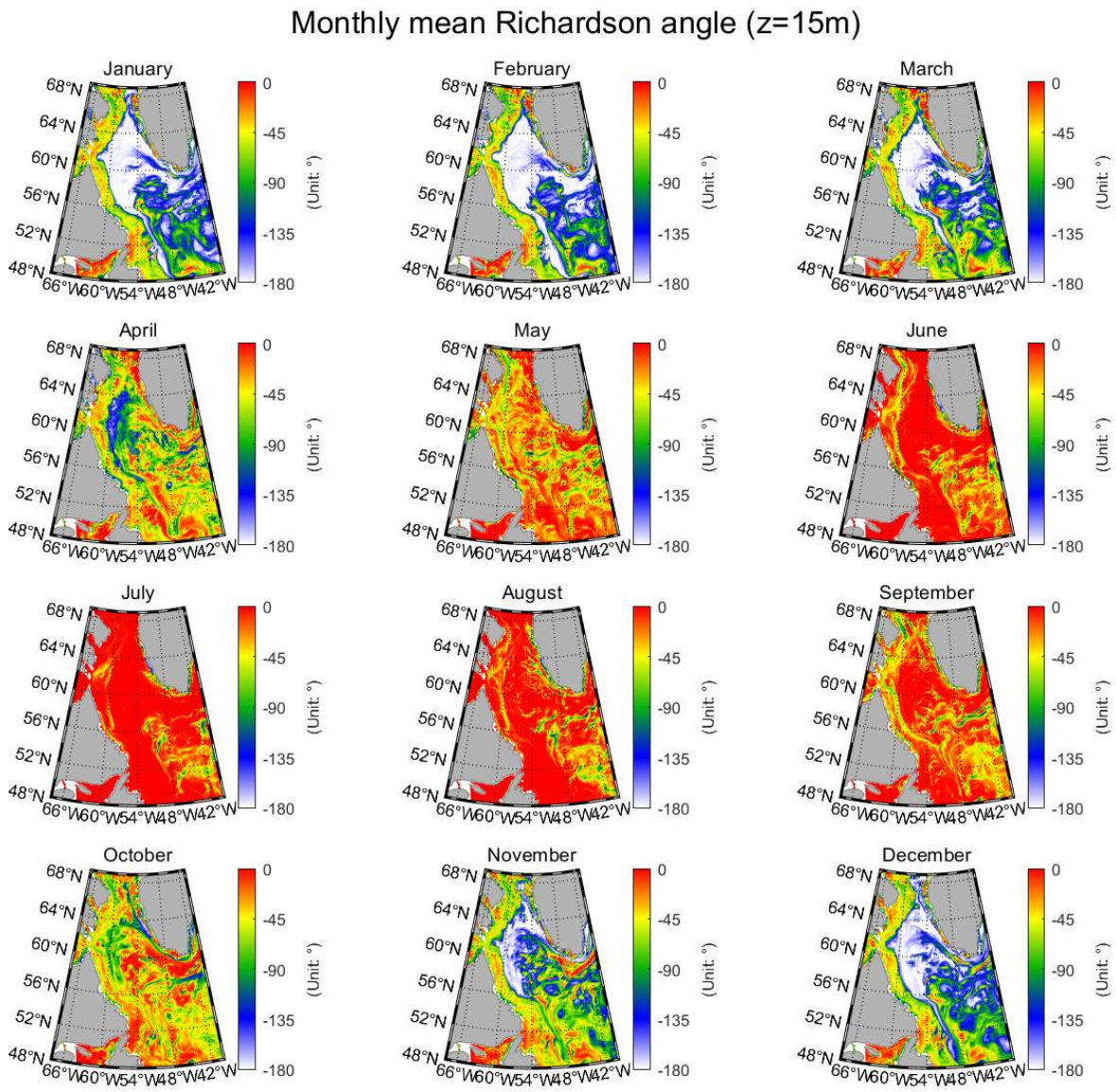

Figure 4.3 Monthly mean Richardson angle (z=15m, plan view)

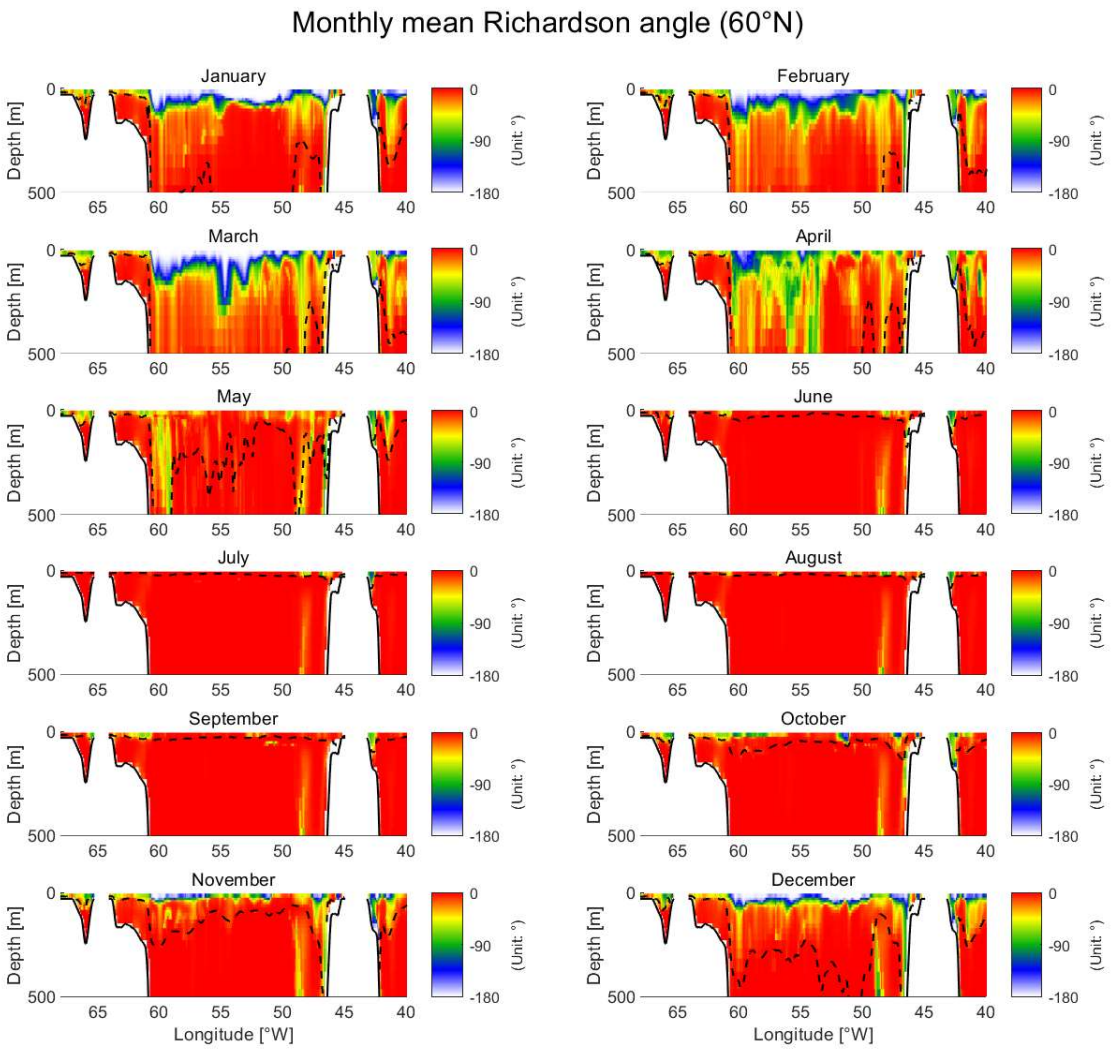

Figure 4.4 Monthly mean Richardson angle near the surface (up to 500m, 60°N, longitudinal view). The MLDs are depicted with dashed lines in the plots.

4.3 Classification and Quantification of Instabilities

The calculated Richardson angle (Figures 4.3 and 4.4) is used to determine the instability type based on the classifications shown in Figure 1.10. The same color code from Figure 1.10 is used for each instability type. Instabilities are displayed for monthly mean fields in Figures 4.5 and 4.6.

Although the Labrador Sea remains widely stable most of the time, various kinds of instabilities develop near the surface by being induced by atmospheric cooling, especially during fall and winter. These instabilities have the same temporal (seasonality) and spatial patterns (large instabilities in the Labrador continental shelves) as the balanced Richardson angle, and almost all instabilities are observed within ML in concurrence with a negative Ertel PV.

The kind of instabilities that develop presents some spatial differences, which are described below.

Firstly, large amount of GI (green) is observed near the surface. GI is generated when the vertically unstable buoyancy gradients are more dominant than the horizontal ones. The occurrence of GI is because the water surface is the interface between the ocean water and atmosphere and the atmospheric forcing is directly transported via this interface.

Secondly, a large amount of SI (yellow) can be seen at water depths between 100m and 300m, and SGI (purple) are located between GI and SI. This is because the atmospheric cooling decreases with depth, and the Richardson angle increases with depth. As the Richardson angle rapidly increases at water depths between 100m and 200m, a small amount of SGI can be seen. In addition to these instabilities, also the ISI appear (grey) but very rarely.

The temporal variation of the above instabilities is well-defined and analogous to that of the Richardson angle. During wintertime (November – March), GI is detected in the whole domain near the surface (0m – 70m) except near continental shelves, while during summertime (April – September), the domain becomes more stable. The Baffin Bay starts to stabilize later than other regions because this region is strongly unstably stratified due to atmospheric cooling. The continental shelves in front of the Baffin Island and Newfoundland Sea are symmetrically unstable throughout the year.

Some instabilities are observed near the bottom, as expected from the obtained results with the Ertel PV and the Richardson angle. However, as prescribed in the previous chapter, there are difficulties to investigate bottom instabilities due to the coarser spatial resolution near the seabed.

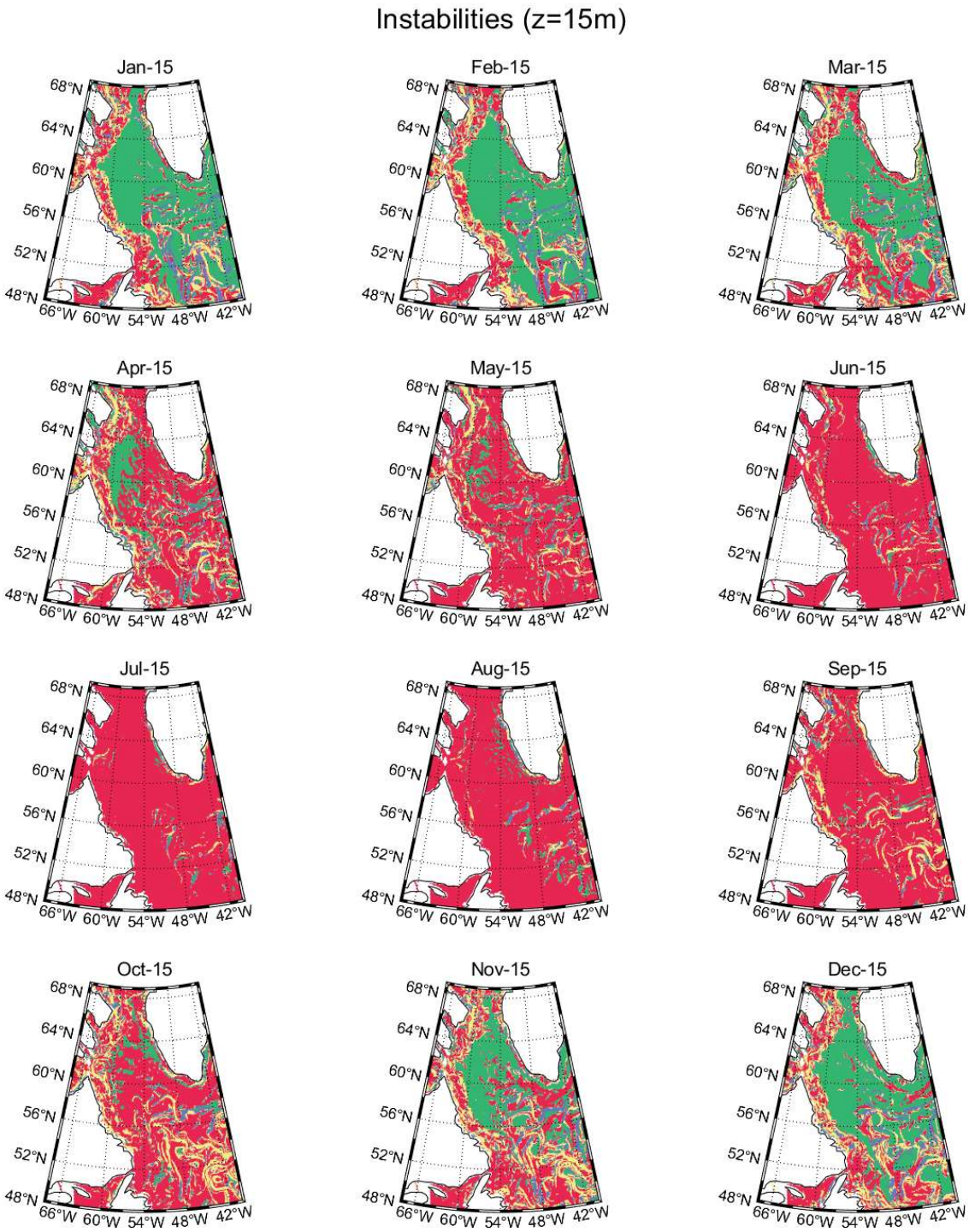

Figure 4.5 Instabilities (z=15m, plan view). The same color code from Figure 1.10 is used for each instability type; Gravitational Instability (GI): green color; Symmetric/Gravitational Instability (SGI): purple color; Symmetric Instability (SI): yellow color; and Inertial/Symmetric Instability (ISI): gray respectively.

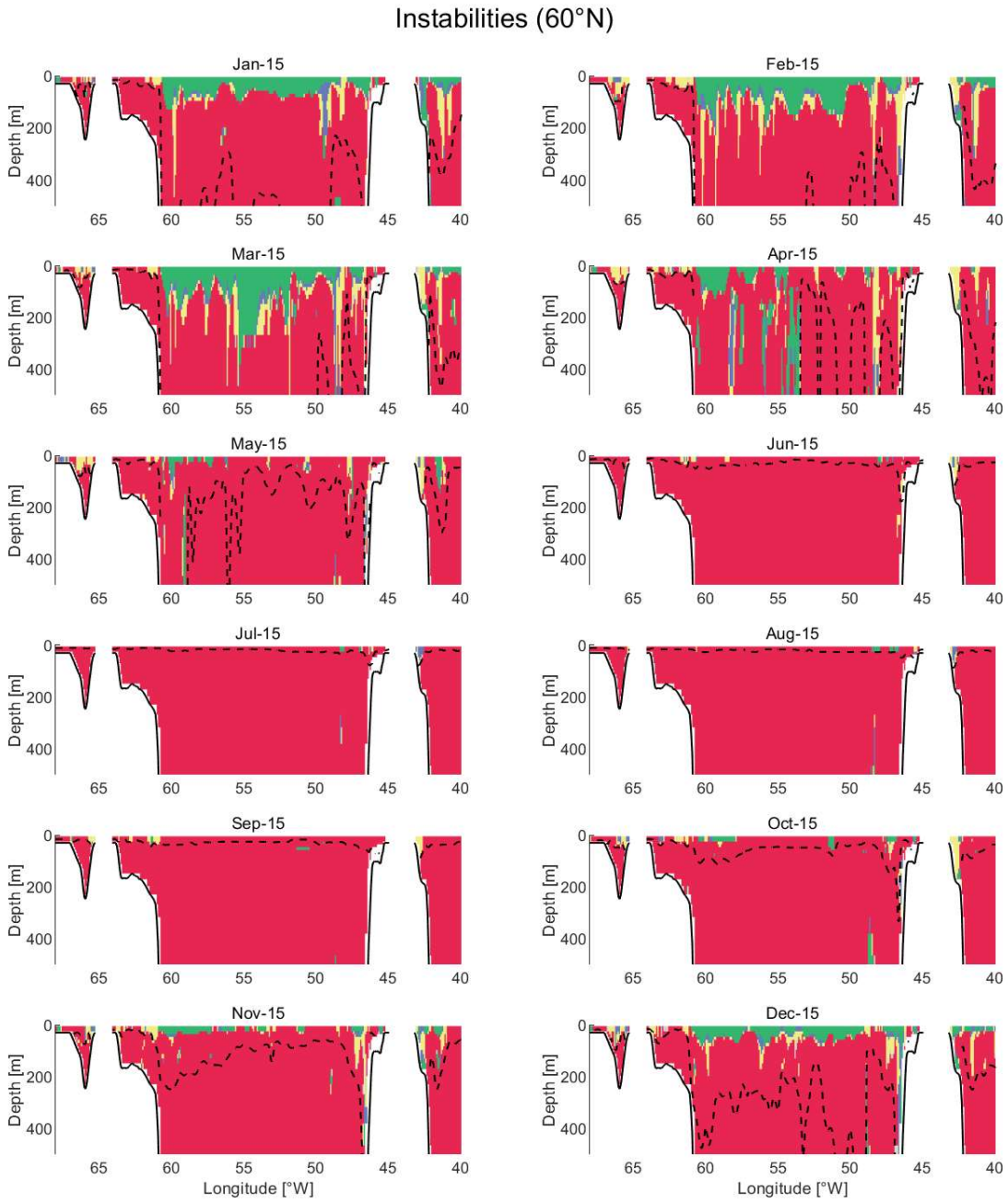

Figure 4.6 Instabilities near the surface (up to 500m, 60°N, longitudinal view). The same color code from Figure 1.10 is used for each instability type; Gravitational Instability (GI): green color; Symmetric/Gravitational Instability (SGI): purple color; Symmetric Instability (SI): yellow color; and Inertial / Symmetric Instability (ISI): gray respectively. The MLDs are depicted with dashed lines in the plots.

4.3.1 Quantifying the Presence of Instabilities

In order to investigate the temporal variability of each type of instability, the volumetric amount of each instability and the Ertel PV are reviewed and compared in Figure 4.7.

To this end, the volume of the grid cell of each instability divided by the total volume of the Labrador Sea for each day of the year is shown in Figure 4.7a. They have a seasonal cycle in which higher values are found in winter and lower values in summer. The largest percentage corresponds to GI, which accounts for from 0.5% to 3.5%, and the second largest is SI, which ranges from 0.2% to 2.1%. The third most frequent instability is SGI, which is below 1% all the time. Finally, the ISI is very scarce (below 0.1%). There is a rebound for GI because of vigorous mixing in March, which can be confirmed from both the lowest value of the Richardson angle (Figure 4.3) and the deepest MLD (Figure 2.4).

The volume of the grid cell of each instability divided by the total volume of the mixed layer in the Labrador Sea for each day of the year are shown in Figure 4.7b. They have the same seasonal cycle as the panel a, but SI dominates GI over summertime (June – October). This is because atmospheric forcing is weak during summertime and the source of GI (unstable stratification) is lost accordingly. The time series includes rebounds during summer season (in June for SI and in September for GI). This is probably because MLD in summertime is very shallow and it occupies only few vertical grid points (sometimes even only 2 points). But the main findings: (1) there are more instabilities in wintertime; and (2) most instabilities exist within MLD (see the different order of magnitude in y-axes) are still valid.

Lastly, Figure 4.7c and d show the percentages of positive and negative Ertel PV over the whole depth and within ML. They also display the same temporal (more negative PV / instabilities in winter) and spatial (more negative PV / instabilities within ML) patterns.

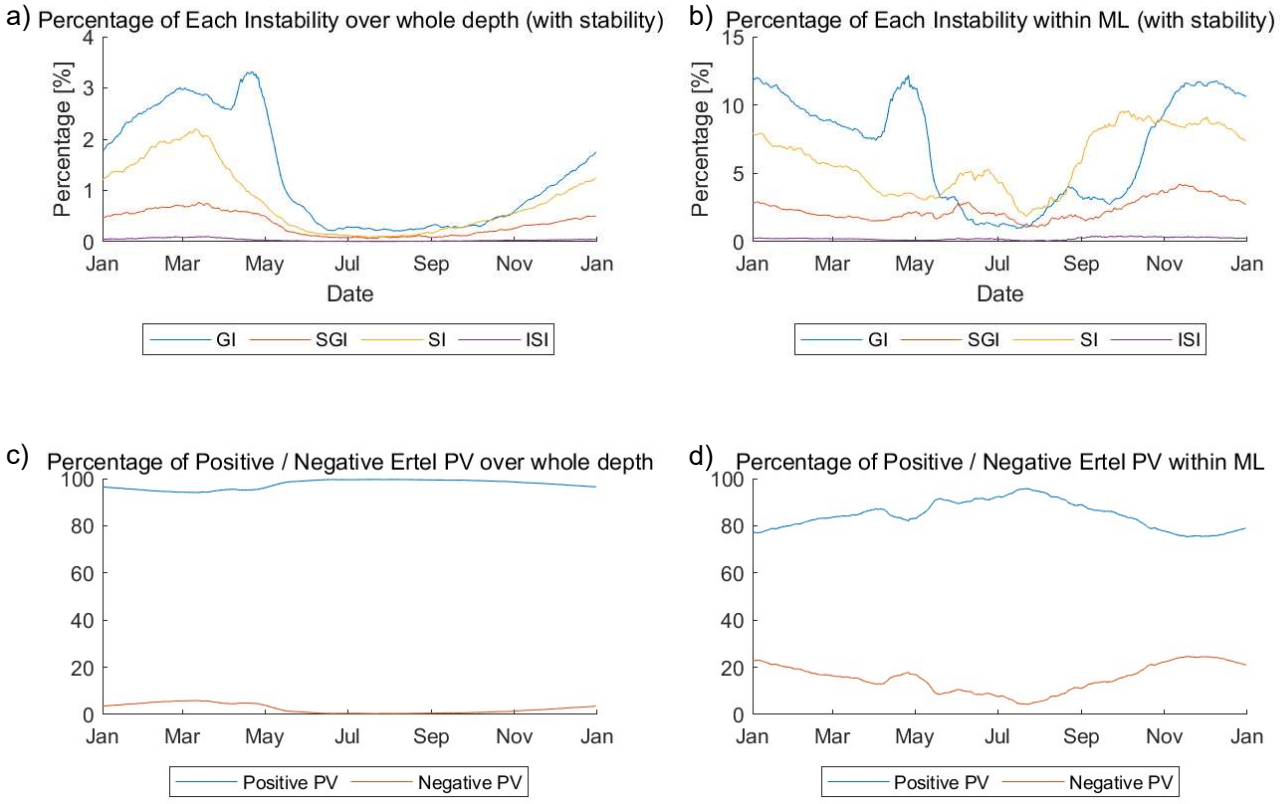

Figure 4.7 Percentages of each instability mode and sign of Ertel potential vorticity. a) The volume of each instability and stability divided by the total volume of the Labrador Sea; b) the volume of each instability divided by the total volume of the mixed layer in the Labrador Sea for each day of the year; c) and d) the percentages of positive and negative Ertel PV over the whole depth and within ML respectively. The abbreviations in the legends are GI: Gravitational Instability; SGI: Symmetric/Gravitational Instability; SI: Symmetric Instability; and ISI: Inertial/Symmetric Instability respectively.

The percentage of each instability mode and the Ertel PV are summarized by averaging time series in Figure 4.7 over time and tabulated in Table 4.1 and 4.2.

	Instability mode	Incl. stability	Excl. stability
Whole depth	Gravitational Instability (GI)	1.32%	52.86%
	Symmetric/Gravitational Instability (SGI)	0.34%	13.67%
	Symmetric Instability (SI)	0.80%	32.05%
	Inertial/Symmetric instability (ISI)	0.04%	1.43%
	Stable	97.51%	
Within MLD	Gravitational Instability (GI)	9.09%	52.68%
	Symmetric/Gravitational Instability (SGI)	2.22%	12.87%
	Symmetric Instability (SI)	5.73%	33.21%
	Inertial/Symmetric instability (ISI)	0.21%	1.23%
	Stable	82.75%	

Table 4.1 Yearly mean volumetric percentage of each type of instability including and excluding the stable area.

	Sign of Ertel PV	Share
Whole depth	Positive PV	97.51%
	Negative PV	2.49%
Within MLD	Positive PV	82.75%
	Negative PV	17.25%

Table 4.2 Yearly mean percentage of positive / negative Ertel PV.

4.4 Summary

The Ertel potential vorticity has a clear seasonality in which a lot of negative values (unstable) can be found during winter season (October – March), while almost the whole domain is stable during summertime. This seasonality can also be seen from the instability mode plots (Figures 4.5 and 4.6). A large amount of instabilities is found during wintertime and it diminishes during summer season. GI is the most frequent instability, followed by SI and SGI. ISI is also present but rarely. These temporal patterns can also be confirmed from the time series shown in Figure 4.7.

Most of instabilities are present within ML, especially near the ocean surface. A significant amount of GI is observed near the surface, and SI is present at water depths between 100m and 300m. SGI is located between GI and SI. The reason is that the water surface is directly affected by the atmospheric forcing and the vertical buoyancy gradient decreases substantially with depth.

The Baffin Bay has a very broad range of the Richardson angle (-180° in winter and 0° in summer), while the remainder provides a relatively narrow range (between -135° and -45°). The Baffin Bay becomes stable later than other regions. This is because the Baffin Bay is strongly affected and unstably stratified by strong atmospheric forcing.

5. Baroclinic Instabilities

The instabilities explained in the previous chapter do not completely release the available potential energy (APE), and the remaining APE may be used as a source for the growth of baroclinic instabilities. If baroclinic instabilities grow enough, it can develop mesoscale eddies of geostrophic scales (from tens to hundreds of km) and may contribute to restratify the ocean.

In this chapter, representative parameters related with the formation of baroclinic instabilities are estimated, and its spatio-temporal patterns are reviewed. These parameters are used to comprehensively describe the full chain of processes behind the mixed layer variability in Chapter 6.

5.1 Eady Growth Rate

The Eady growth rate represents the possibility that a location becomes baroclinically unstable. This growth rate can be obtained by applying the linear quasi-geostrophic approach, characterized by large vertical and lateral shears. However, it is very laborious to solve the linear quasi-geostrophic stability calculations and, it requires a numerical solver. Instead, a simplified formula for the maximum Eady growth rate can be used, which is defined as (Isachsen 2015):

$$\omega_{Eady}^{Max} = 0.3\frac{|U_{tw}|}{L_d} \tag{5.1}$$

where U_{tw} is the top-to-bottom thermal wind shear and L_d is the first internal deformation radius. Both are expressed as:

$$U_{tw} = \int_{-H}^{0} \frac{\partial U}{\partial z} dz \tag{5.2}$$

$$L_d = \frac{1}{f}\int_{-H}^{0} N dz \tag{5.3}$$

where, U is the horizontal background velocity, and L_d, the first internal deformation radius is similar to the internal Rossby radius (see Eq 5.4), but L_d is π times bigger than the Rossby radius.

The Brunt–Väisälä frequency (N) is determined by the square root of the vertical density gradient, and the vertical density gradient may be negative in the upper ocean layer due to strong winter convection. Accordingly, the Brunt–Väisälä frequency can be imaginary and this leads to a complex number for the Eady growth rate. Eady (1949) assumed stable stratification and constant Brunt–Väisälä frequency in his derivation, hence the imaginary Eady growth rate has no useful physical sense. Therefore, the imaginary part is ignored.

Figure 5.1 shows the monthly mean Eady growth rate in a plan view. The Eady growth rate is much larger on the continental shelves (ranges from 3 to above 20 day^{-1}), especially where a steep bathymetric slope is found. The interior Labrador Sea has relatively lower values (around 0.1 day^{-1}) than those from the continental shelves.

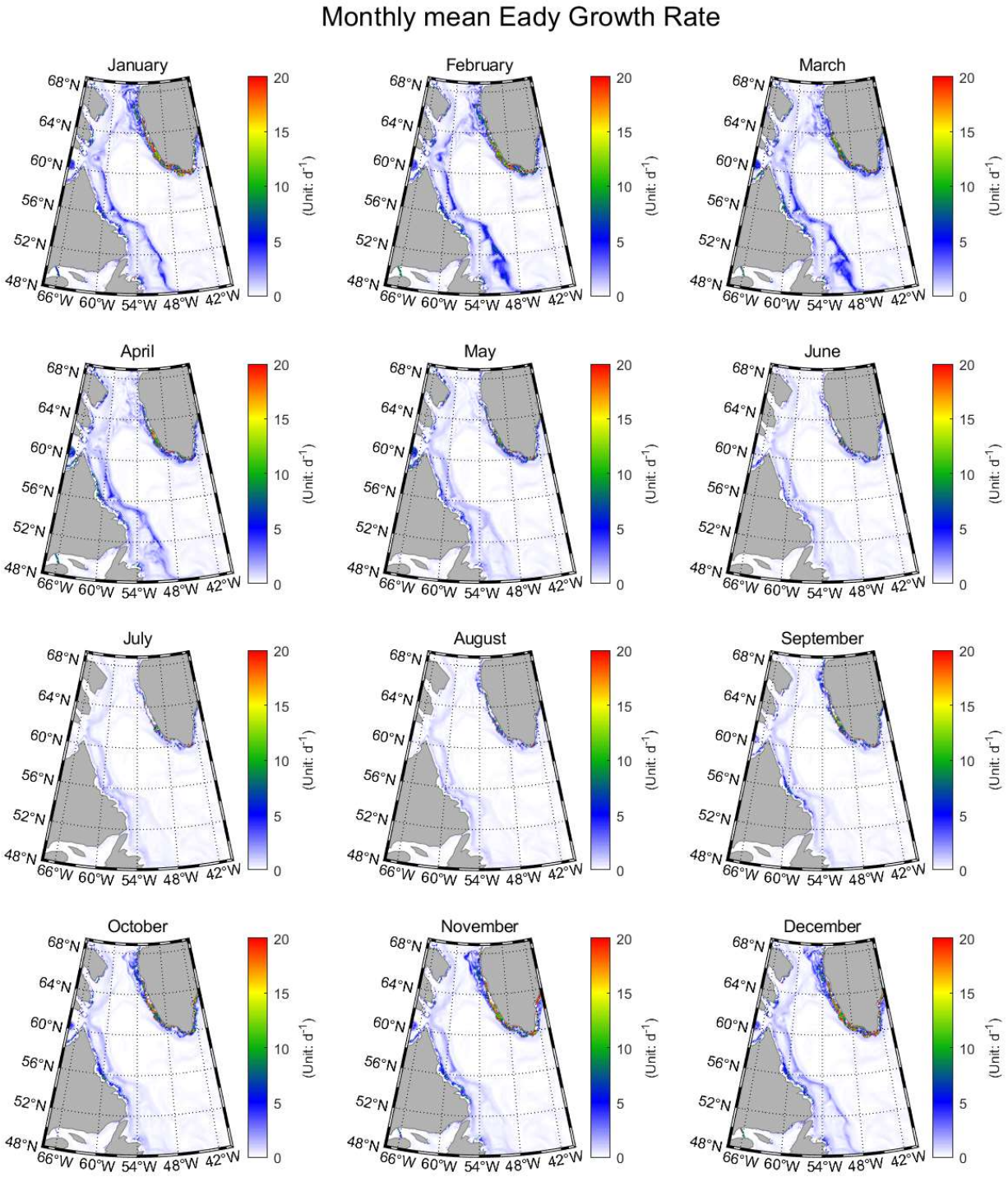

Figure 5.1 Monthly mean Eady growth rate.

Because the Eady growth rate has very different magnitudes with locations, its temporal variation is investigated with the basin-averaged time series in Figure 5.2. It shows relatively low values during summer season, especially around August (about 0.4 day^{-1}), and larger values during wintertime, reaching its peak (about 1.2 day^{-1}) in February.

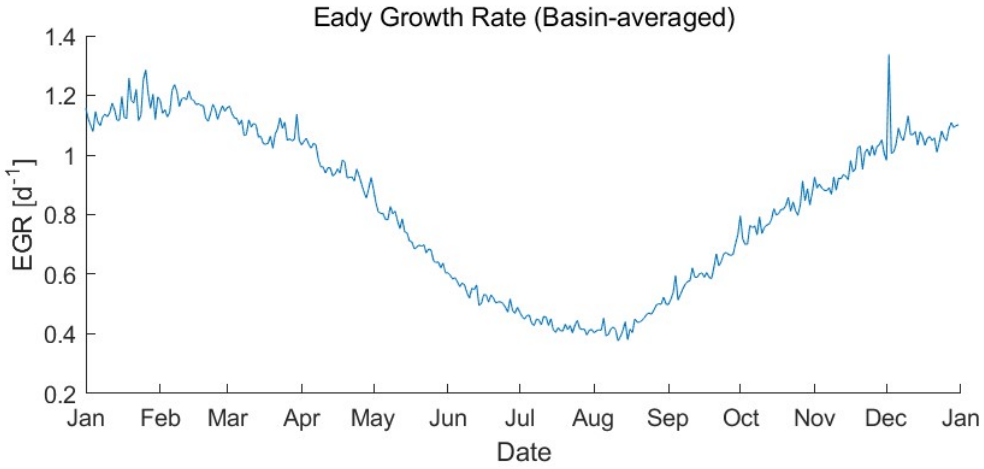

Figure 5.2 Basin-averaged Eady growth rate time series.

5.2 Internal Rossby Radius

The internal Rossby radius of baroclinic deformation is of crucial importance in oceanography. The Rossby radius is the horizontal scale at which rotation effects become as important as buoyancy effects (Nurser et al. 2014), and it sets the final size of developed baroclinic instabilities that have become eddies.

The internal Rossby radius can be obtained by solving the linearized quasi-geostrophic potential vorticity equation for zero background mean flow (Chelton et al. 1998), but it can be simplified as:

$$R_i = c_i/|f| \tag{5.4}$$

where, i is the baroclinic mode, f is the Coriolis parameter and c_i is the long Rossby wave speed. The later can be expressed as:

$$c_i = (\pi i)^{-1} \int_{-H}^{0} N \, dz \tag{5.5}$$

where $N = \sqrt{\frac{-g}{\rho_0}\frac{\partial \rho}{\partial z}}$ is the Brunt–Väisälä frequency (unit: s^{-2}). In this computation, only the first baroclinic mode is considered because the higher order baroclinic modes require a finer model resolution.

The Rossby radius also requires the Brunt–Väisälä frequency, hence imaginary numbers appear again. The Rossby radius is the horizontal scale at which the geostrophic balance becomes as important as buoyancy effects, and stable stratification was assumed when it was derived. Therefore, this imaginary Rossby radius has no relevant physical meaning. In this study, the imaginary part of the Rossby radius is ignored.

Figure 5.3 shows the monthly mean Rossby radius in a plan view.

There are several notable spatial features in the Rossby radius results. First, around Newfoundland Sea the Rossby radius is larger (larger than 20km) due to the lower latitude and the larger bottom depths. Second, the Labrador Sea is characterized by a smaller Rossby radius than in the Newfoundland Sea, which ranges between 8km and 12km. The Baffin Bay and the continental shelves in the domain have very small Rossby

radius. This is because of the shallow water depth which limits the growth of eddy size due to the slow Rossby wave speed.

Temporal patterns are similar for the whole domain. From June to October, the Rossby radius is larger than during other months, and it decreases from December. This is because the ocean is well-stratified from December, hence the Rossby wave speed is faster than during other seasons. These temporal patterns are confirmed by the basin-averaged time series in Figure 5.4.

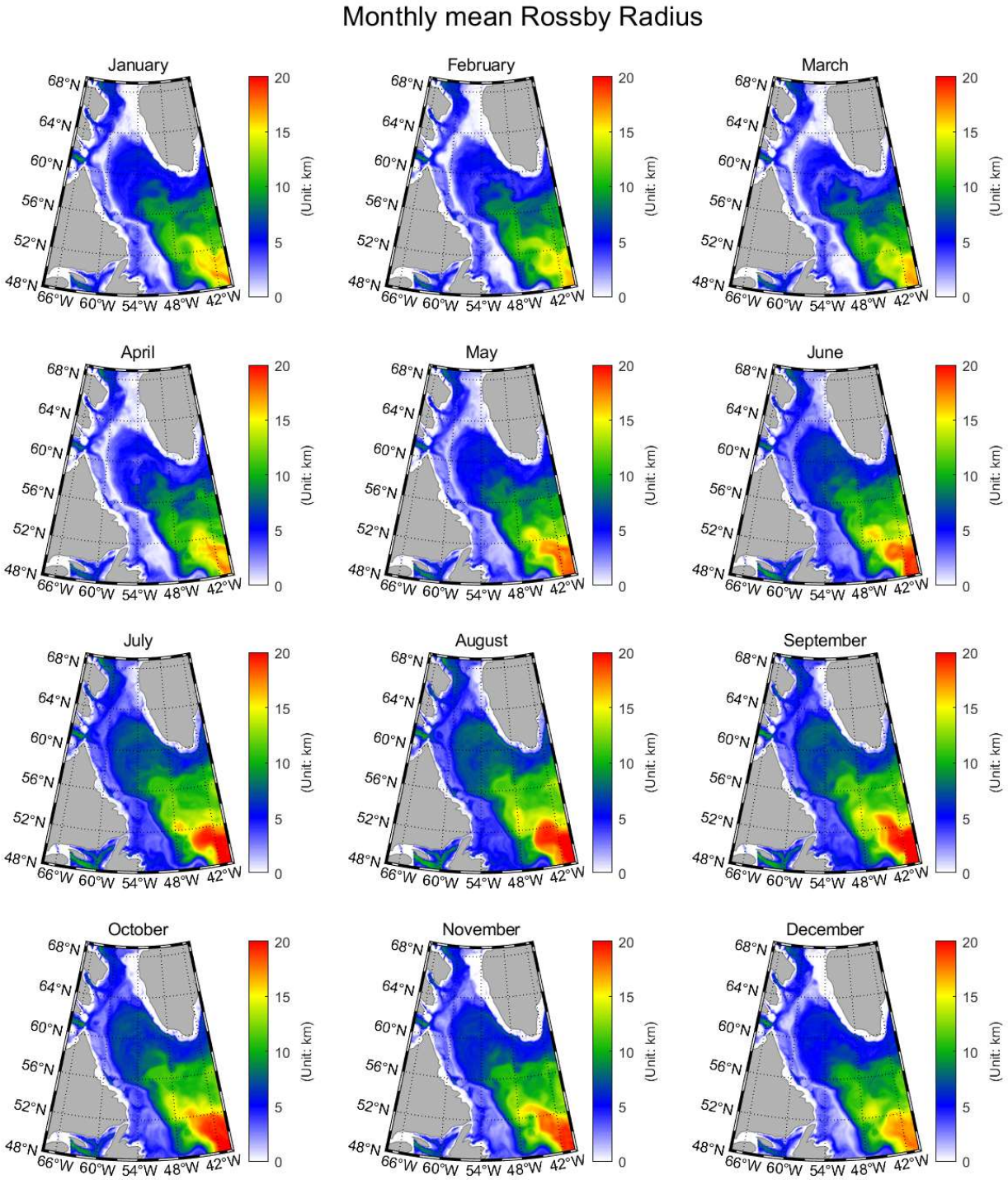

Figure 5.3 Monthly mean internal Rossby radius.

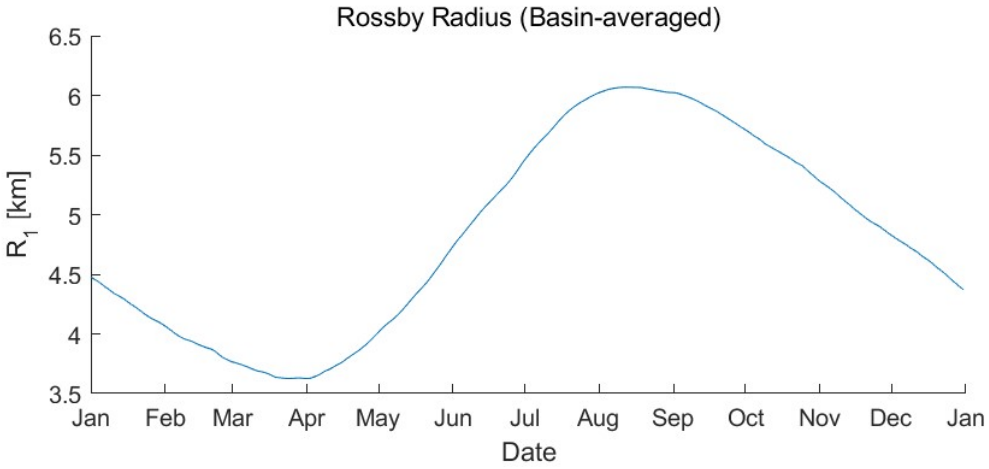

Figure 5.4 Basin-averaged internal Rossby radius time series.

5.3 Eddy Kinetic Energy

The eddy kinetic energy (EKE) is one of the crucial parameters to assess the energy status for baroclinic instabilities in the ocean. EKE is a useful measure for several reasons: first, if EKE is larger or of the order of the mean flow then the role of eddies is considered significant in driving the flow (Holland et al. 1983). Second, spatial patterns of EKE give clues to identify sources and sinks of energy. Third, horizontal eddy mixing is approximately proportional to EKE (Price 1982). Hence, by acquiring a better understanding of the spatial variations of eddy mixing it is possible to better forecast the distribution of ocean tracers (Richardson 1983).

The eddy kinetic energy (EKE) is expressed as:

$$EKE = \frac{1}{2}[(u-\bar{u})^2 + (v-\bar{v})^2 + (w-\bar{w})^2] \tag{5.6}$$

where, u, v and w are the zonal (x direction), meridional (y direction) and vertical (z direction) velocity (m/s) respectively, and $\bar{u}$, $\bar{v}$ and $\bar{w}$ are the yearly mean velocities for the zonal, meridional and vertical directions respectively.

Figure 5.5 shows the monthly mean EKE in the Labrador Sea. High EKE can be seen in the Newfoundland Sea, on the border between the Baffin Bay and the Labrador Sea (around 54°W, 62°N) and around the continental shelves in the Labrador Peninsula and the Baffin Island. These regions are where large eddy activities occur (eddy hotspots, see Figure 5.7), and it can be said that the effects of baroclinic instability are most vigorous in these regions.

The temporal patterns of EKE are shown in the basin-averaged time series in Figure 5.6. Clearly, higher EKE is seen especially in April and May, and the EKE is low from August to October. These temporal patterns can also be confirmed in Figure 5.5.

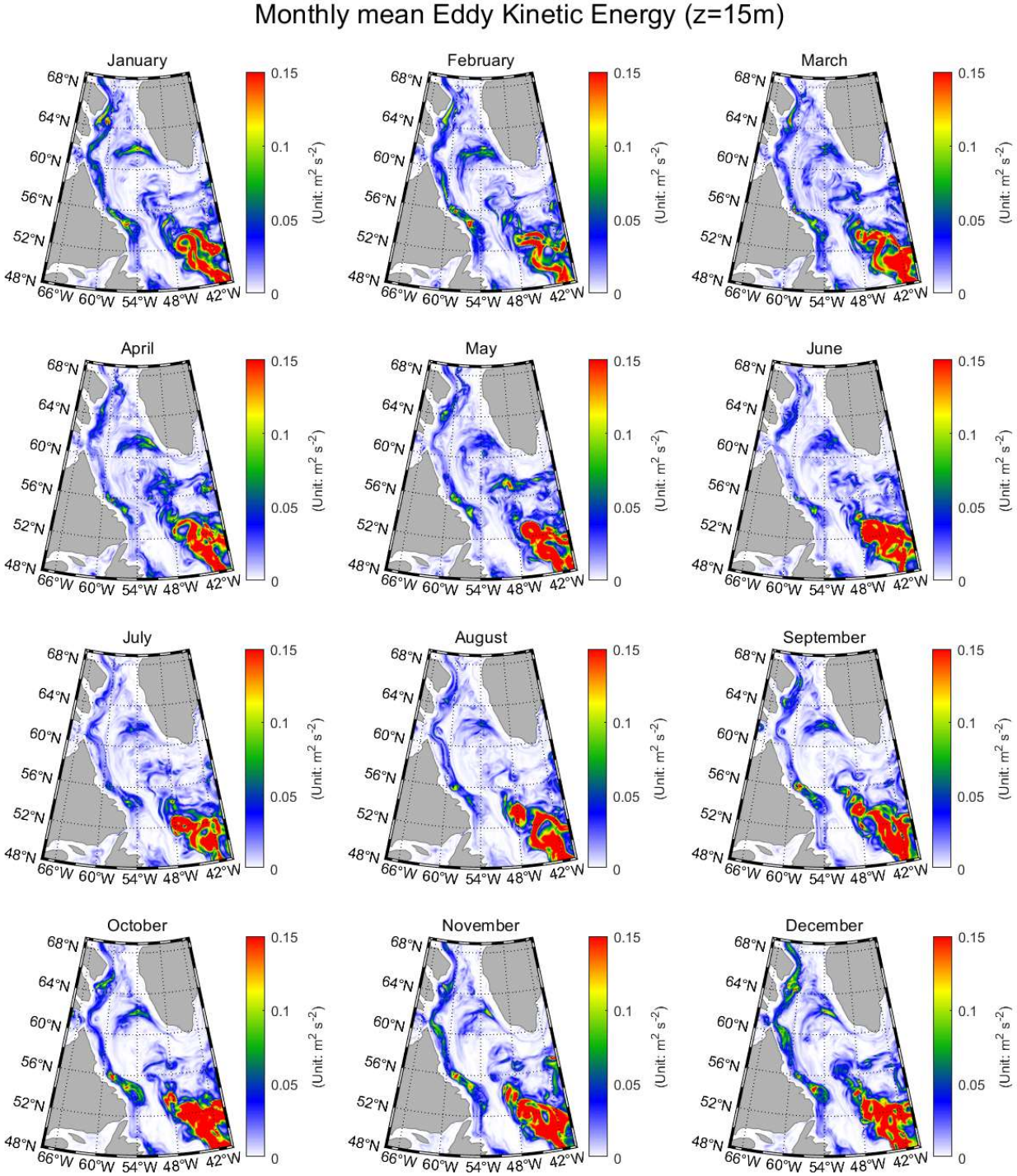

Figure 5.5 Monthly mean eddy kinetic energy (z=15m, plan view).

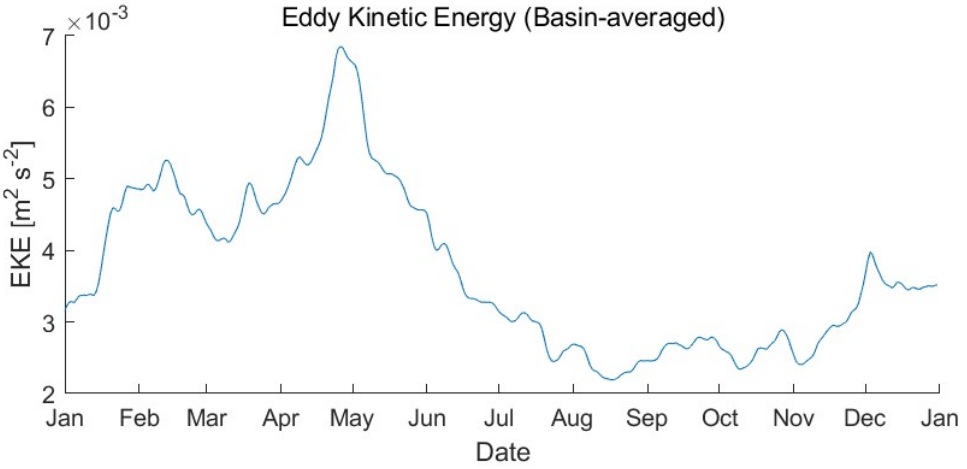

Figure 5.6 Basin-averaged eddy kinetic energy time series.

5.4 Okubo-Weiss Parameter

The Okubo-Weiss parameter is a very common measure to identify ocean eddies. it is expressed as (Williams et al. 2011):

$$OW = s_n^2 + s_s^2 - \omega^2 \tag{5.7}$$

where, $s_n = \frac{\partial u}{\partial x} - \frac{\partial v}{\partial y}$, $s_s = \frac{\partial v}{\partial x} + \frac{\partial u}{\partial y}$ and $\omega = \frac{\partial v}{\partial x} - \frac{\partial u}{\partial y}$.

That is, the Okubo-Weiss parameter is composed of (1) normal strain (s_n), (2) shear strain (s_s) and (3) relative vorticity (ω). When the Okubo-Weiss parameter is positive it is strain-dominated and when it is negative the location is vorticity-dominated.

A disadvantage of this parameter is that for those numbers close to zero it is affected by noise. In order to filter out this noise, an extended approach is to divide the Okubo-Weiss values by their standard deviation (normalization) and consider the calculation meaningful if it is smaller than -0.2 (threshold).

Because this Okubo-Weiss parameter does not contain rotating direction information or eddy polarity (cyclonic or anti-cyclonic), the rotating directions is added by multiplying by sign of vorticity as a final step i.e.:

$$OW_{this\ study} = \left|OW_{filtered}\right| \times sign(\omega) \tag{5.8}$$

Figure 5.7 shows the Okubo-Weiss parameter for each month. It clearly shows cyclonic eddies (positive values, red color) and anti-cyclonic eddies (negative values, blue color). This figure displays several features: (1) the presence of eddies in the Labrador Sea all throughout the year; (2) it shows a similar temporal patterns to the basin-averaged EKE (see Figure 5.6), meaning that relatively few eddies are found from August to October and the largest numbers of eddies are present in April and May; (3) size of eddies estimated by the internal Rossby radius is also confirmed by the Okubo-Weiss parameter.

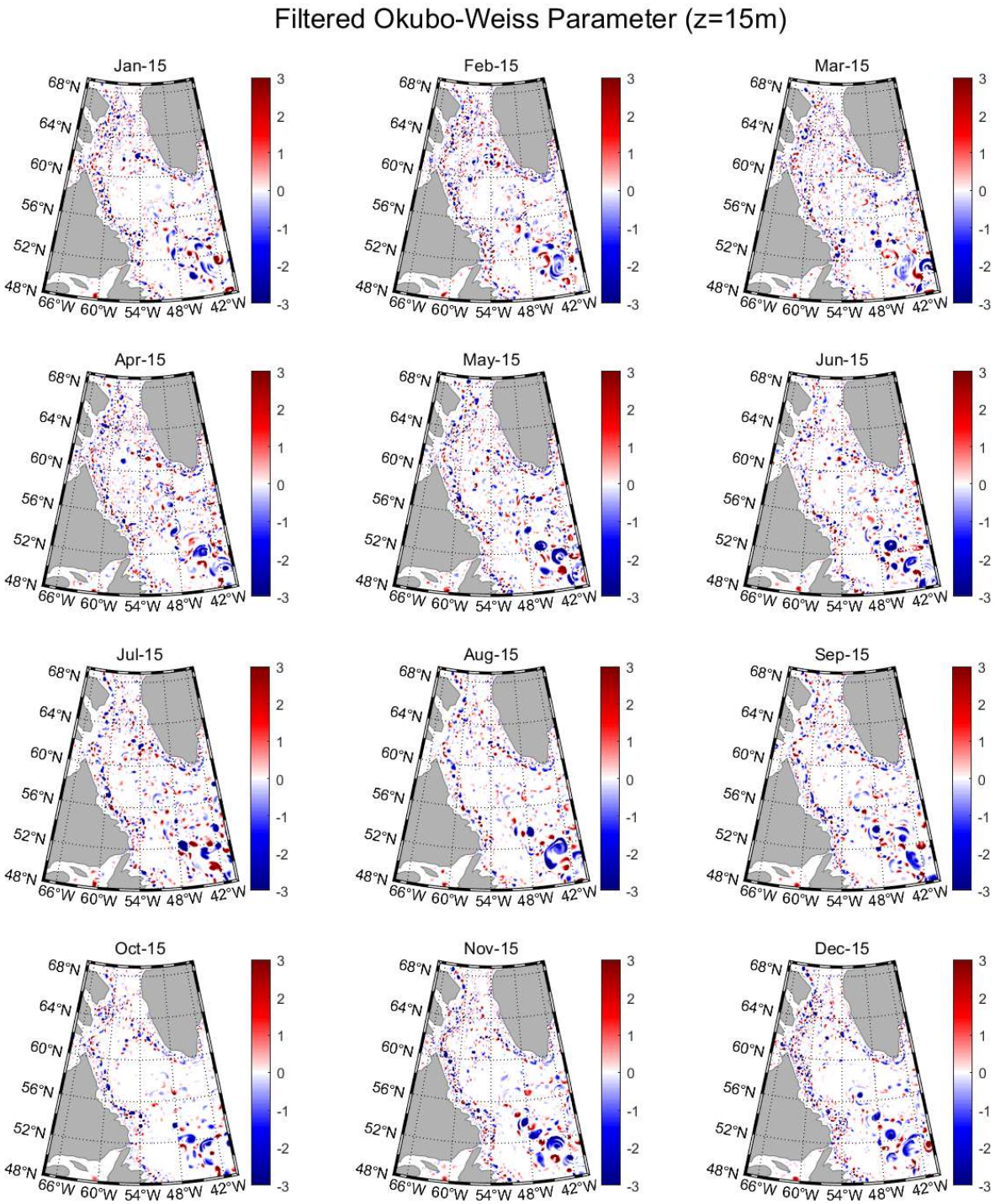

Figure 5.7 Filtered Okubo-Weiss Parameter (z=15m, plan view). The color shading presents cyclonic eddies (red); anti-cyclonic eddies (blue).

5.5 Summary

During winter season, the Eady growth rate responds quickly to the atmospheric cooling and convection processes. The Eady growth rate shows its peak in around February (Figures 5.1 and 5.2). In this regard, note that the Eady growth rate is related with the presence of baroclinic instabilities not with the presence of already formed coherent mesoscale eddies. Therefore, it is not surprising that the strongest eddy activity is present in May (Figures 5.5 and 5.6), while the largest eddy growth occurs in February, which is likely a counteracting response to the developing instabilities induced by winter convection and already discussed in Chapter 4.

It is inferred from the Eady growth rate that eventually a lot of eddies are formed on the continental shelves in the Labrador Sea (Figure 5.1) but eddies likely immediately leave the place where they are formed and wander to other areas of the Labrador Sea and its surroundings. A large number of eddies are found in the domain, but eddies are present especially in the Newfoundland Sea, on the border between the Baffin Bay and the Labrador Sea (around 54°W, 62°N) and around the continental shelves in the Labrador Peninsula and the Baffin Island (Figures 5.5 and 5.7).

To conclude, the internal Rossby radius shows the spatial and temporal variations in eddy size (Figures 5.3 and 5.4), which have also been confirmed by the Okubo-Weiss parameter (Figure 5.7).

6. Comprehensive Analysis

In the previous chapters, various energetic and dynamic magnitudes related to the MLD variability have been reviewed respectively. This chapter investigates the connection between all these magnitudes. This aims to provide better understanding about seasonal MLD variability, linking winter convection with late spring/summer restratification. To this end, several representative locations have been selected.

In order to provide the hypothesis on the full chain of processes, several parameters are investigated, which are: (1) Eady growth rate; (2) Eddy Kinetic Energy; (3) Energy Ratio; (4) the presence of eddies according to the Okubo-Weiss parameter; (5) gravitational and/or symmetric instability type; (6) Richardson angle; and (7) Mixed Layer Depth are investigated. Based on a careful analysis of those magnitudes, it is possible to describe, at first order, the cause-effect mechanisms that induce the MLD seasonal variability in the Labrador Sea. This is a general description especially for the deep Labrador basin, and this can differ among locations.

1. As a consequence of the winter atmospheric-induced cooling, gravitational and/or symmetric instabilities start to develop in the upper ocean layers. Those instabilities drive intense water movement thus breaking the stratification and favoring energy conversion from the available potential energy (APE) to kinetic energy (KE) (i.e. more mixing). However, this response is far from being homogeneous, as it depends on the local dynamics, the bathymetry and on the water-mass properties.
2. If the above processes persist with time, water mass properties start to become vertically more uniform and the MLD deepens. Interestingly, the spatially unequal mixing favors the formation of more sloping isopycnals, which are a source of baroclinic instabilities (Figure 6.1). Therefore, these instabilities start to grow to flatten again the isopycnals, which is reflected by the strong Eady growth during mid-winter.
3. However, this increase in baroclinic instabilities is not able to overcome the still strong atmospheric-induced gravitational and/or symmetric instabilities until winter comes to the end. Therefore, there is not a straightforward relationship between Eady growth and MLD.
4. When spring arrives, the simultaneous effect of the end of convection together with the increase in the number of mesoscale eddies helps to restratify the Labrador Sea thus shallowing the MLD and completing the MLD seasonal cycle.

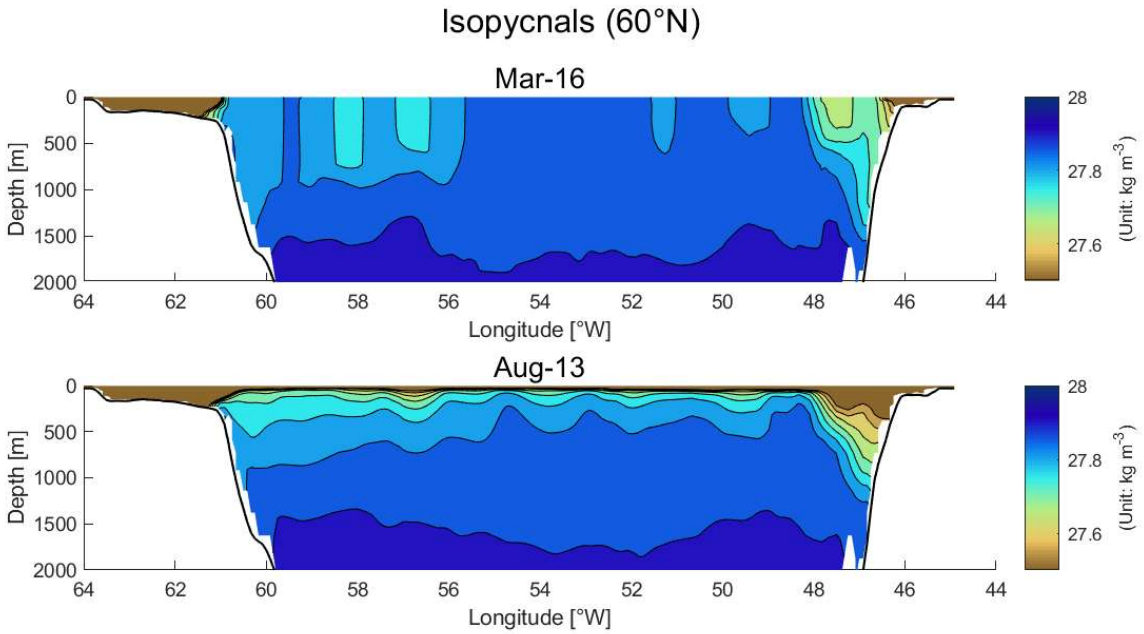

Figure 6.1 Isopycnals for (a) winter season; and (b) summer season.

6.1 Temporal Variability

In order to look into more details about this set of processes, several locations are selected based on the outcomes in the previous chapters, which are (1) deep mixed layer depth, (2) high eddy kinetic energy, (3) high Eady growth rate, and (4) high eddy activity determined by the Okubo-Weiss parameter. Table 6.1 shows the subject locations for the comprehensive analysis.

#	Location	Selected Based On
1	54.67°W, 59.83°N	Deep Mixed Layer Depth
2	53.75°W, 62.17°N	High Eddy Kinetic Energy
3	58.67°W, 56.67°N	High Eady Growth Rate
4	48.00°W, 60.00°N	Vigorous Eddy Activity determined by the Okubo-Weiss parameter

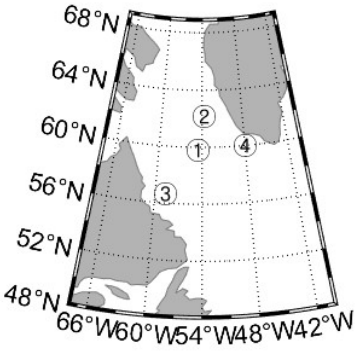

Table 6.1 Subject locations for the comprehensive analysis.

Figures 6.2 to 6.5 show the time series of (a) the Eady growth rate and the Eddy Kinetic Energy; (b) the Energy Ratio, eddies detected by the Okubo-Weiss parameter and gravitational and/or symmetric instability type; (c) the Richardson angle and the Mixed Layer Depth for selected locations.

6.1.1 Location 1

Figure 6.2 effectively shows the role of gravitational and/or symmetric instabilities on the chain of processes behind the MLD variability. From the beginning of the time series, a large amount of gravitational instability develops (lower part of in Figure 6.2 b) which is induced by atmospheric forcing, and the MLD gradually deepens (Figure 6.2 c) and considerable wiggles can be found on ERs (Figure 6.2 b). In May, gravitational instability is no longer present at this location and the MLD starts to gradually shallow.

The effects of baroclinicity are not clear as baroclinic instability is not well developed at this location. This is because the mixing is equally done in space, isopycnals are relatively horizontal (see Figure 6.1 a). This low baroclinicity can be confirmed by the low Eady growth rate and eddy kinetic energy (Figure 6.2 a).

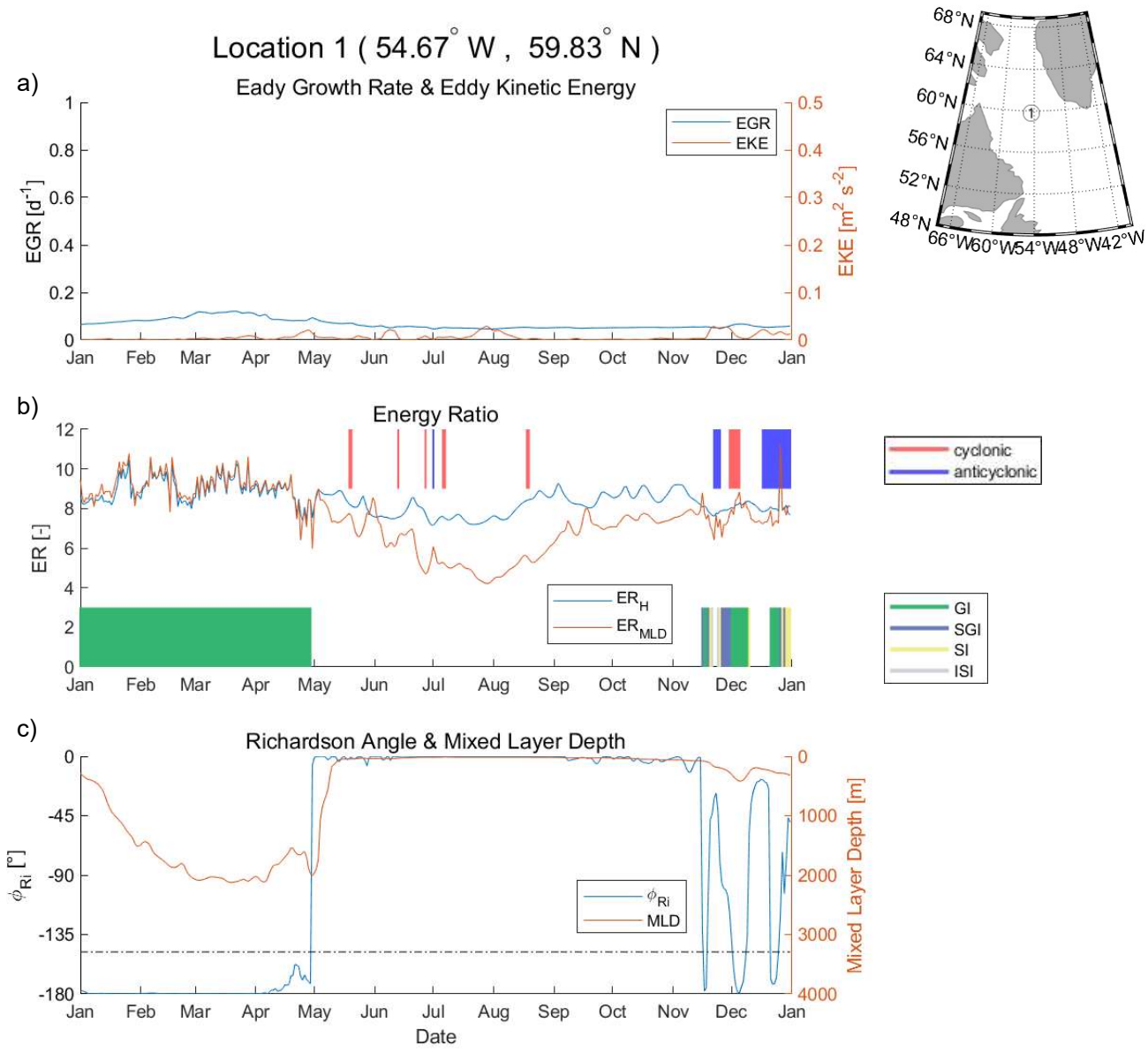

Figure 6.2 Time series for Location 1 (see inset figure) of (1) the Eady growth rate and basin-averaged eddy kinetic energy; (2) energy ratio for the whole water depth and within ML; (3) the Richardson angle and MLD. The existence of instabilities is marked in the lower part of the second plot. The color shading mimics the one of Figure 1.10; Gravitational Instability (GI): green color; Symmetric/Gravitational Instability (SGI): purple color; Symmetric Instability (SI): yellow color; and Inertial / Symmetric Instability (ISI): gray respectively. Existence of eddies perceived by the Okubo-Weiss parameter is marked in the upper part of the second plot. Red color represents cyclonic eddies and blue color represents anti-cyclonic eddies. Dash-dotted line represents the water deph for this location.

6.1.2 Location 2

Figure 6.3 more effectively displays the competing between gravitational and/or symmetric instabilities and baroclinic instabilities. During winter season (January – March), a large amount of gravitational and/or symmetric instabilities (especially GI) develops (lower part of in Figure 6.3 b), and the MLD deepens as a response of gravitational and/or symmetric instabilities (Figure 6.3 c). However, vigorous eddy activity occurs at this location (see large eddy detection in the upper part of Figure 6.3 b and high EKE in Figure 6.3 a) and disturbs the MLD development (The MLD is not well developed unlike that in Figure 6.2). After symmetric instability diminished, the MLD becomes shallow.

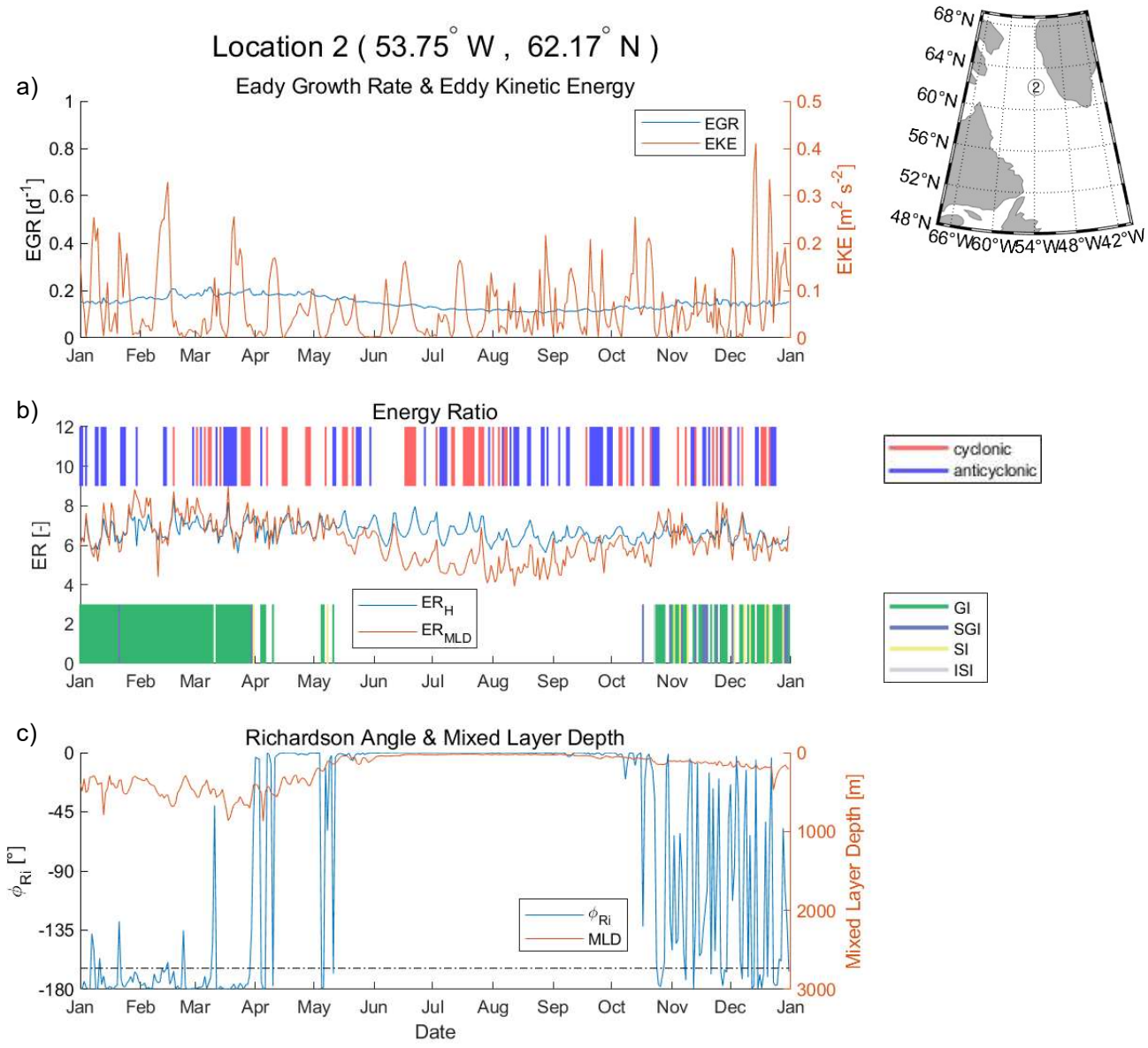

Figure 6.3 As Figure 6.1, but for Location 2 (see inset figure).

6.1.3 Location 3

Location 3 is the most hydraulically variable location because of the shallow water depth and steep bathymetric slope. At this location, gravitational and/or symmetric instabilities and eddies are present all throughout the year (upper and lower part of in Figure 6.4 b). Because of this active gravitational and/or symmetric instabilities and baroclinic instability, daily fluctuations of the MLD and the Richardson angle are extreme (panel c), and this location does not follow the hypothesis very well. Note that the range of y-axis for the Eady growth rate (Figure 6.4a) is larger than in previous locations.

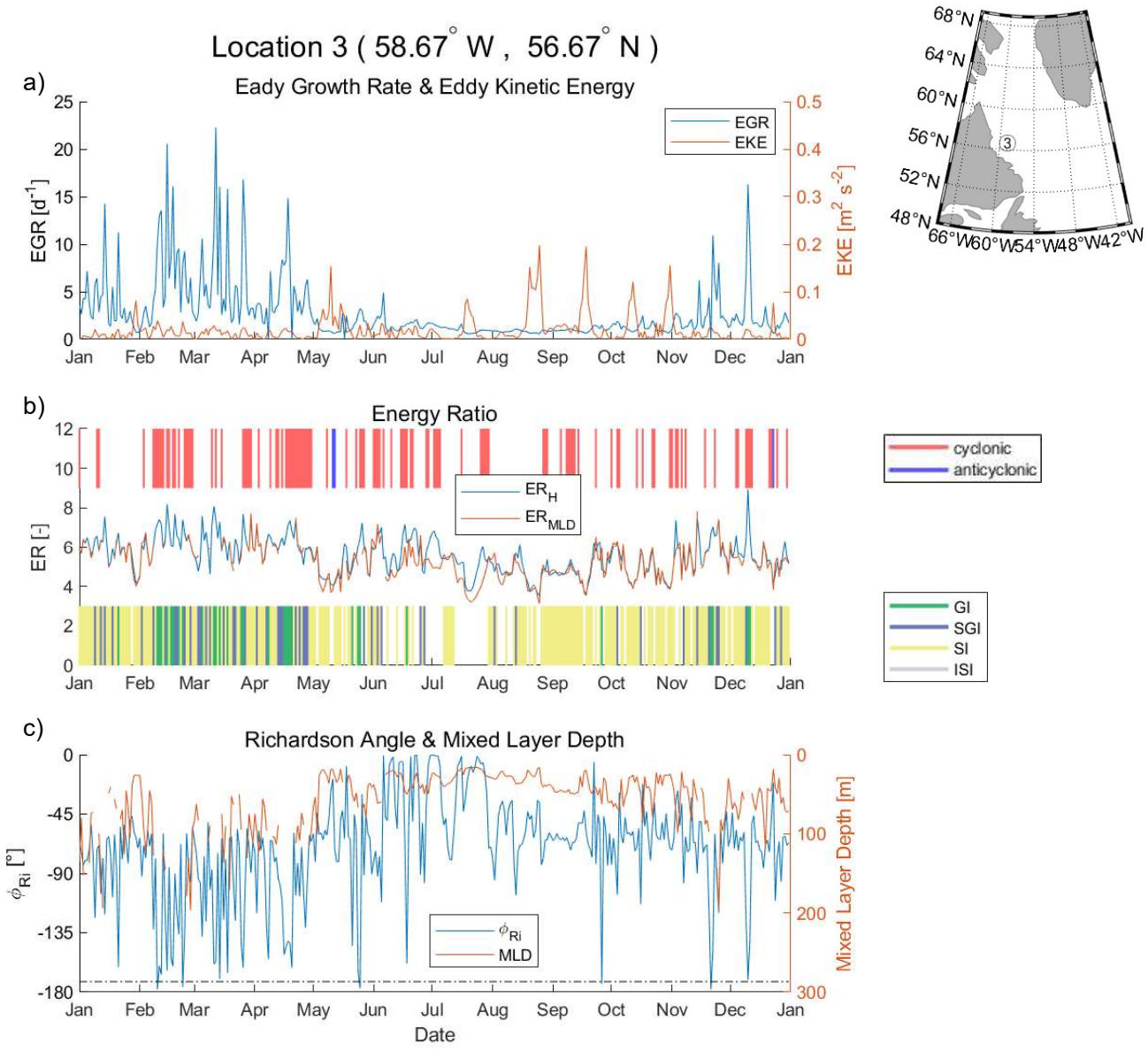

Figure 6.4 As Figure 6.1, but for Location 3 (see inset figure). Note that the range of y-axis for the Eady growth rate is much broader and higher than in Figures 6.2, 6.3 and 6.4.

6.1.4 Location 4

Figure 6.5 shows the time series for the so-called 'eddy hotspot' clearly shows the role of baroclinic instability on the chain of processes behind the MLD variability. Despite of the existence of gravitational and/or symmetric instabilities, the MLD is not well developed due to active eddy activities.

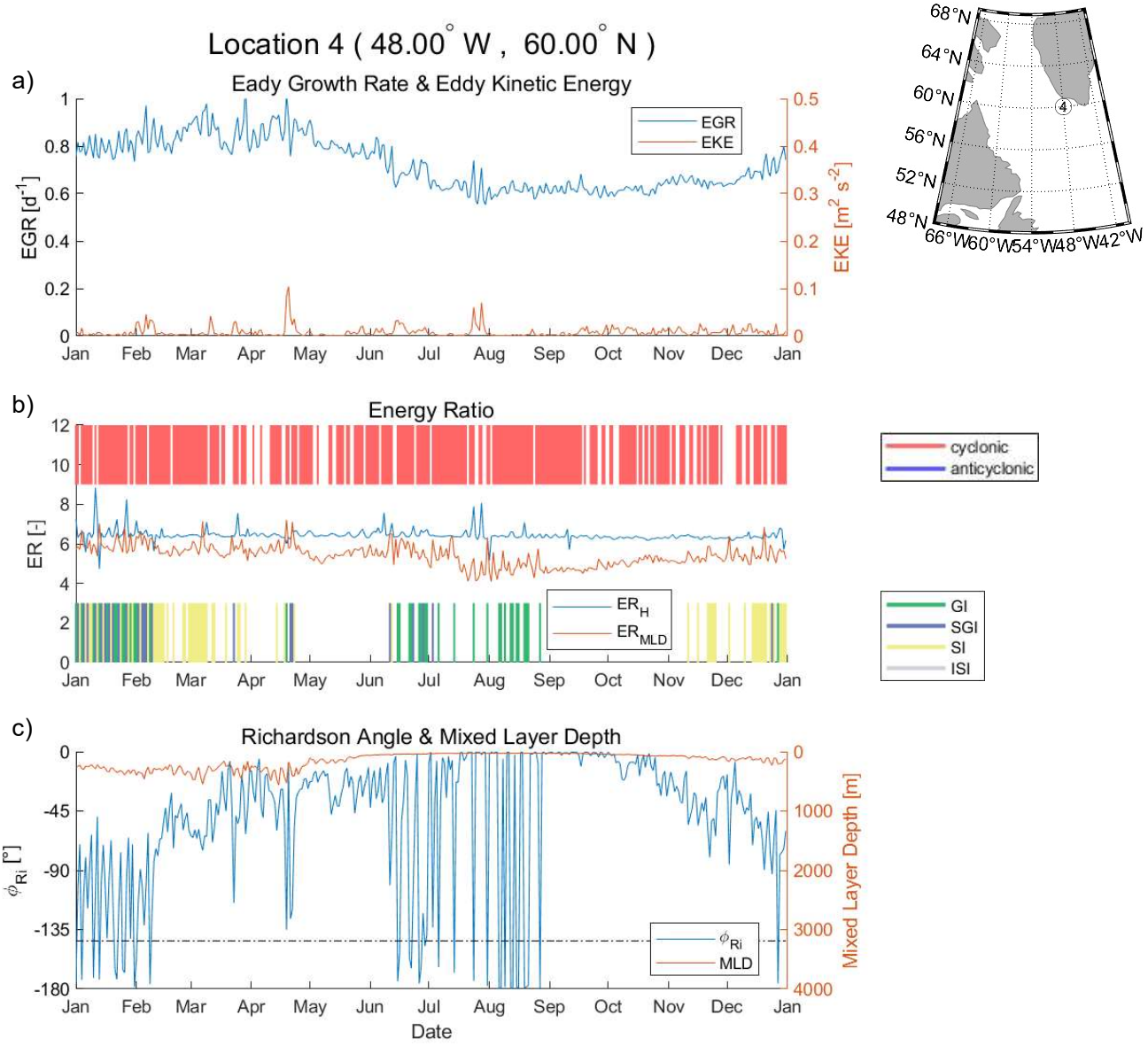

Figure 6.5 As Figure 6.1, but for Location 4 (see inset figure).

7. Conclusion & Recommendations

This chapter summarizes the answers for the research questions investigated in this study. It is followed by some recommendations to extend the present work.

7.1 Answers to Research Questions

Which is the best method to compute the mixed layer depth in the Labrador Sea?

Mixed layer depths (MLD) were estimated with various threshold values of potential temperature and potential density, and their spatial and temporal patterns were investigated. The computed MLDs were compared with an Argo float gridded climatology, and the best threshold method to compute MLDs was determined.

Those MLDs computed with the smaller threshold values ($\Delta\theta = 0.2℃$ and $\Delta\sigma_\theta = 0.03\ kg\ m^{-3}$) were shallower, while larger threshold values ($\Delta\theta = 0.5℃$ and $\Delta\sigma_\theta = 0.1\ kg\ m^{-3}$) provided even as deep MLDs as almost the whole column of water depth reaching the bottom at some points. The spatial patterns of four methods were considerably similar, but the larger thresholds often generated abrupt changes in temporal patterns and the smaller thresholds were smoother and more reasonable.

The density-based MLDs can be said more credible values because buoyancy changes may also be driven by salinity differences, not only by temperature. Temperature-based MLDs are a complementary metric and a valid alternative when density data are not available.

In terms of reduction of the data, it has been shown that a median provides shallower MLDs and is a more appropriate statistical estimator in good agreement with de Boyer Montégut et al. (2004), who indicated that the mean is often skewed toward higher values.

Where and when does the highest conversion between potential and kinetic energies occur?

The spatial and temporal patterns of energy conversion were investigated by means of the available potential energy (APE) and kinetic energy (KE). To better track the relative variations between APE and KE, the Energy Ratio (ER) was introduced, which is defined as a logarithm of the ratio between the vertically integrated APE and KE. Besides this study also defined the ER for the whole depth (ER_H), not only for the MLD (ER_{MLD}).

One key result is that patterns of ER were similar to those of yearly MLD, especially in the center of the Labrador Sea where the deepest MLD was observed and in the southwest part of Greenland where West Greenland Current flows. ER_H was roughly constant over the year, while ER_{MLD} displayed a seasonality that lower values in summertime (May – October). This can be interpreted as that because a large amount of APE within the ML is released by vigorous mixing during wintertime, and the remaining APE is very little within the ML in summer.

The energy conversion was more clearly shown by the temporal variation of the ERs. As an example, at a location in the deep Labrador basin, large temporal variations were found during wintertime (January – April), and the temporal variation was smoother in summer, which demonstrated that much more vigorous energy conversion occurs in winter than summer. In contrast, for a location around an eddy hotspot, the ER depicted more wiggles and ER_{MLD} deviates from ER_H more than location a due to the high KE by vigorous eddy activity.

How do the absolute vorticity and the vertical and horizontal buoyancy gradients behave in the Labrador Sea? What kind of instabilities can be identified from the imbalances between the absolute vorticity and buoyancy gradients? How do they change in space and time?

The Ertel potential vorticity provided a lot of negative values (indicating the presence of instabilities) during mid fall/winter (October – March) and positive values (stable) in the whole domain in mid spring/summer (April – September). Most instabilities existed within ML, especially near the ocean surface. This was expected as a large buoyancy loss is driven by the strong atmospheric-induced winter cooling.

Also, some negative values were found near the bottom. This was likely due to the shear stress generated by bottom friction. However, there were some difficulties to investigate details of these instabilities because the boundary layer is much thinner than the vertical grid size.

Various kinds of instabilities developed, and the instabilities occurred near the surface during winter season. Large amount of GI (see Table 1.4) was found near the surface, and a large amount of SI developed at water depths between 100m and 300m. SGI were located between GI and SI. This was because the atmospheric forcing is directly transported via the water surface and decreases with depth, which can be inferred by the vertical patterns of the Richardson angle. ISI also appear but very rarely.

GI was detected in the whole domain near the surface (0m – 70m) except in continental shelves during wintertime (November – March), while the domain became stable during summertime (April – September). The Baffin Bay started becoming stable later than other regions because this region is strongly unstably stratified by atmospheric cooling. The continental shelf in front of the Baffin Island and Newfoundland Sea were symmetrically unstable throughout the year.

How do ocean eddies affect the restratification of the upper layers?

During winter season, the Eady growth rate responded quickly to the atmospheric cooling and convection processes. The Eady growth rate showed its peak in around February. In this regard, note that the Eady growth rate is related with the presence of baroclinic instabilities not with the presence of already formed coherent mesoscale eddies. Therefore, it was not surprising that the strongest eddy activity was present in May, while the largest eddy growth occurred in February, which was likely a counteracting response to the developing gravitational and/or symmetric instabilities induced by winter convection.

It was inferred from the Eady growth rate that eventually a lot of eddies were formed on the continental shelves in the Labrador Sea but eddies likely immediately left the place where they were formed and wandered to other areas of the Labrador Sea and its surroundings. A large number of eddies were found in the domain, but eddies were present especially in the Newfoundland Sea, on the border between the Baffin Bay and the Labrador Sea (around 54°W, 62°N) and around the continental shelves in the Labrador Peninsula and the Baffin Island.

To conclude, the internal Rossby radius showed the spatial and temporal variations in eddy size, which have also been confirmed by the Okubo-Weiss parameter.

How do these processes interact? What comprehensive patterns can we observe?

We could infer the chain of processes behind the MLD variability, and the hypothesis was summarized below. This is a general description for the deep Labrador basin, and this can differ among locations.

1. As a consequence of the winter atmospheric-induced cooling, gravitational and/or symmetric instabilities start to develop in the upper ocean layers. Those instabilities drive intense water

movement thus breaking the stratification and favoring energy conversion from the available potential energy (APE) to kinetic energy (KE). However, this response is far from being homogeneous, as it depends on the local dynamics, the bathymetry and on the water-mass properties.

2. If the above processes persist with time, water mass properties start to become vertically more uniform and the MLD deepens. Interestingly, the spatially unequal mixing favors the formation of more sloping isopycnals, which are a source of baroclinic instabilities. Therefore, these instabilities start to grow to flatten again the isopycnals, which is reflected by the strong Eady growth during mid-winter.
3. However, this increase in baroclinic instabilities is not able to overcome the still strong atmospheric-induced gravitational and/or symmetric instabilities until winter comes to the end. Therefore, there is not a straightforward relationship between Eady growth and MLD.
4. When spring arrives, the simultaneous effect of the end of convection together with the increase in the number of mesoscale eddies helps to restratify the Labrador Sea thus shallowing the MLD and completing the MLD seasonal cycle.

7.2 Recommendations

In this study, the physical processes behind the MLD seasonal variability in the Labrador Sea are analyzed. Roughly, MLD seasonality is determined by the competition between gravitational and/or symmetric instabilities (which aid to vertically mix the ocean or to reduce the potential vorticity) and baroclinic instabilities (which aid to restratify the ocean or increase the potential vorticity). This section suggests some recommendations to further extend this study.

7.2.1 Horizontal Model Resolution

This study analyzes the physical processes with a high-resolution model data (1/12° × 1/12°). However, the model resolution still needs to become finer because the model does not properly resolve meso- and submesoscale instabilities yet. It is known that if the ratio of the internal Rossby radius to a model's grid-diagonal distance is smaller than 2, eddy parameterizations are needed (Hallberg 2013).

Figure 7.1 shows the ratio of model's grid-diagonal distance to the yearly mean internal Rossby radius from this study. The figure shows several features: (1) the entire domain has a ratio smaller than 2, hence the model resolution still needs to be finer; (2) around the continental shelves, especially in front of the Labrador Peninsula and Greenland, this ratio has extremely small values (around 0.2). This is because the continental shelves have very small Rossby radius as those regions have very shallow water depth which limits the growth of eddy size due to the slow Rossby wave speed. The continental shelves are of importance in baroclinic development and a number of eddies are observed in these regions. Hence, a higher resolution model data is needed in analyzing the physical processes behind MLD variability, especially instabilities.

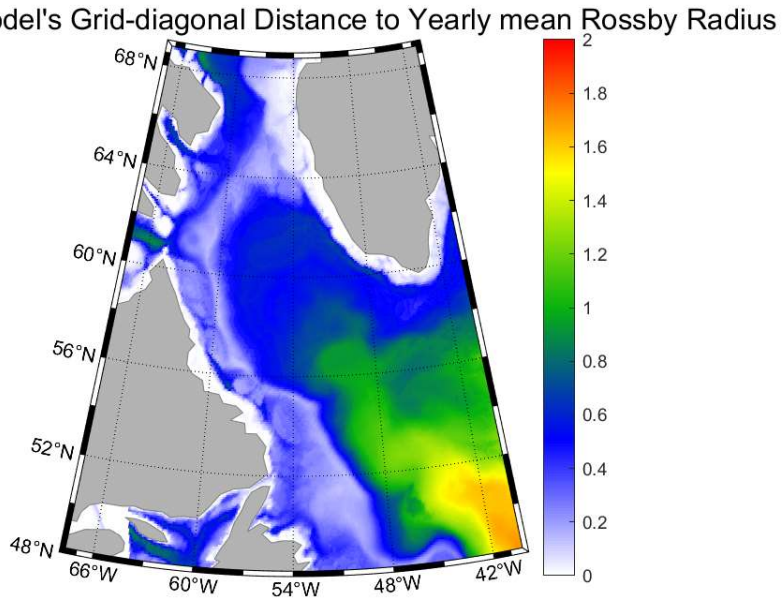

Figure 7.1 Ratio of model's effective grid spacing to the yearly mean internal Rossby radius.

7.2.2 Vertical Model Resolution

During the instability analysis with the Ertel potential vorticity, some instabilities are found near the bottom. This is likely due to the shear stress generated by bottom friction, which may intensify under a significant bathymetric slope as it occurs at the southern side of Greenland.

As the vertical grid spacing gradually increases with depth, the vertical grid size near the bottom (250m) is much thicker than the boundary layer, which is typically of the order of meters to tens of meters (Trowbridge et al. 2018). Hence, there are difficulties in investigating details of these instabilities.

If the finer vertical grid size is applied for deeper water depths, the characteristics of these bottom instabilities could be analyzed.

7.2.3 Freshening of the Labrador Sea

The seawater density is a key parameter in the processes behind the MLD variability in the Labrador Sea. It is determined by the several circumstances e.g. cold airflows over the ocean surface, saline water supply from the Irminger Sea, and freshwater discharge from the surrounding land is also one of the key circumstances.

Due to the increasing mass loss of the Greenland ice sheet since the 1990s, the freshwater discharge is expected to increase in subarctic Atlantic in the near future (Böning et al. 2016). This increasing freshwater fluxes may lead to a suppression of winter convection in the Labrador Sea with potential decreases for the strength of the AMOC. Hence, the spatial and temporal patterns of the processes analyzed in this study may differ in this suppressing condition of winter convection. The change in spatial and temporal patterns of the instabilities and in energy exchanges can be analyzed in a follow-up study.

7.2.4 Weakening of the Boundary Current System

A weakening of the Labrador boundary current system in the 1990s was found by direct current-meter observations (Häkkinen et al. 2004). Because the boundary current is a pathway to tranport saline water from the Irminger Sea to open Atlantic ocean, it may affect the deep winter convection in the Labrador Sea. Not only that, because a large amount of baroclinicity is developed along the boudary current, it is one of key systems affecting the MLD variability. Therefore, it is advised to analyze the impacts of this boundary current change on the deep winter convection and baroclinic instability patterns.

7.2.5 More Realistic Atmospheric forcing

The dataset analyzed in this study is generated using a repeated annual cycle from the Coordinated Ocean Reference Experiment (CORE) dataset for the atmospheric forcing (wind, heat fluxes and precipitation) (Large et al. 2004), with the 6-hourly forcing averaged to monthly. This monthly mean field data does not properly represent extreme weather events as extreme values of variables are diminished during averaging processes.

The winter ocean convection and instabilities explained in this study are strongly affected and driven by the extreme weather events. In case of extreme conditions, the use of daily wind and heat fluxes would contribute to a more accurate representation of the physical processes involved in the mixed layer response, including the energy conversion and the developing instabilities.

List of Acronyms

AMOC	Atlantic Meridional Overturning Circulation
APE	Available Potential Energy
CORE	Coordinated Ocean Reference Experiment
EKE	Eddy Kinetic Energy
ER	Energy Ratio
GI	Gravitational Instability
ISI	Inertial/Symmetric Instability
KE	Kinetic Energy
LSW	Labrador Sea Water
ML	Mixed Layer
MLD	Mixed Layer Depth
PE	Potential Energy
PGI	Pure Gravitational Instability
PII	Pure Inertial Instability
POP	Parallel Ocean Program
PV	Potential Vorticity
SGI	Symmetric/Gravitational Instability
SI	Stratification Index
SI	Symmetric Instability

Bibliography

Adcroft, A., C. Hill and J. Marshall (1997). "Representation of topography by shaved cells in a height coordinate ocean model." Monthly Weather Review **125**(9): 2293-2315.

Böning, C. W., E. Behrens, A. Biastoch, K. Getzlaff and J. L. Bamber (2016). "Emerging impact of Greenland meltwater on deepwater formation in the North Atlantic Ocean." Nature Geoscience **9**(7): 523.

Brainerd, K. E. and M. C. Gregg (1995). "Surface mixed and mixing layer depths." Deep Sea Research Part I: Oceanographic Research Papers **42**(9): 1521-1543.

Brunnabend, S.-E. and H. A. Dijkstra (2017). "Asymmetric response of the Atlantic Meridional Ocean Circulation to freshwater anomalies in a strongly-eddying global ocean model." Tellus A: Dynamic Meteorology and Oceanography **69**(1): 1299283.

Calow, P. P. (2009). Blackwell's concise encyclopedia of environmental management, John Wiley & Sons.

Chelton, D. B., R. A. DeSzoeke, M. G. Schlax, K. El Naggar and N. Siwertz (1998). "Geographical variability of the first baroclinic Rossby radius of deformation." Journal of Physical Oceanography **28**(3): 433-460.

Courtois, P., X. Hu, C. Pennelly, P. Spence and P. G. Myers (2017). "Mixed layer depth calculation in deep convection regions in ocean numerical models." Ocean Modelling **120**: 60-78.

Curry, R. G., M. S. McCartney and T. M. Joyce (1998). "Oceanic transport of subpolar climate signals to mid-depth subtropical waters." Nature **391**(6667): 575.

de Boyer Montégut, C., G. Madec, A. S. Fischer, A. Lazar and D. Iudicone (2004). "Mixed layer depth over the global ocean: An examination of profile data and a profile-based climatology." Journal of Geophysical Research: Oceans **109**(C12).

Eady, E. T. (1949). "Long waves and cyclone waves." Tellus **1**(3): 33-52.

Georgiou, S., C. G. van der Boog, N. Brüggemann, S. L. Ypma, J. D. Pietrzak and C. A. Katsman (2019). "On the interplay between downwelling, deep convection and mesoscale eddies in the Labrador Sea." Ocean Modelling **135**: 56-70.

Gill, A. E. (1982). Atmosphere-Ocean Dynamics, Academic Press.

Häkkinen, S. and P. B. Rhines (2004). "Decline of subpolar North Atlantic circulation during the 1990s." Science **304**(5670): 555-559.

Haine, T. W. and J. Marshall (1998). "Gravitational, symmetric, and baroclinic instability of the ocean mixed layer." Journal of physical oceanography **28**(4): 634-658.

Hallberg, R. (2013). "Using a resolution function to regulate parameterizations of oceanic mesoscale eddy effects." Ocean Modelling **72**: 92-103.

Holland, W., D. Harrison and A. Semtner (1983). Eddy-resolving numerical models of large-scale ocean circulation. Eddies in marine science, Springer**:** 379-403.

Holte, J., L. D. Talley, J. Gilson and D. Roemmich (2017). "An Argo mixed layer climatology and database." Geophysical Research Letters **44**(11): 5618-5626.

Hoskins, B. (1974). "The role of potential vorticity in symmetric stability and instability." Quarterly Journal of the Royal Meteorological Society **100**(425): 480-482.

Isachsen, P. E. (2015). "Baroclinic instability and the mesoscale eddy field around the Lofoten Basin." Journal of Geophysical Research: Oceans **120**(4): 2884-2903.

Large, W. G. and S. G. Yeager (2004). "Diurnal to decadal global forcing for ocean and sea-ice models: the data sets and flux climatologies."

Lavender, K. L., R. E. Davis and W. B. Owens (2000). "Mid-depth recirculation observed in the interior Labrador and Irminger seas by direct velocity measurements." Nature **407**(6800): 66.

Lazier, J., R. Hendry, A. Clarke, I. Yashayaev and P. Rhines (2002). "Convection and restratification in the Labrador Sea, 1990–2000." Deep Sea Research Part I: Oceanographic Research Papers **49**(10): 1819-1835.

Nurser, A. and S. Bacon (2014). "The rossby radius in the Arctic Ocean." Ocean Science **10**(6): 967-975.

Pawlowicz, R. (2019). M_Map: A mapping package for MATLAB. available online at www.eoas.ubc.ca/~rich/map.html.

Pickart, R. S., M. A. Spall and J. R. Lazier (1997). "Mid-depth ventilation in the western boundary current system of the sub-polar gyre." Deep Sea Research Part I: Oceanographic Research Papers **44**(6): 1025-1054.

Pickart, R. S., D. J. Torres and R. A. Clarke (2002). "Hydrography of the Labrador Sea during active convection." Journal of Physical Oceanography **32**(2): 428-457.

Price, J. (1982). "Particle dispersion in the western North Atlantic." Unpublished manuscript, Woods Hole Oceanographic Institution, Woods Hole MA **2543**.

Price, J. F., R. A. Weller and R. Pinkel (1986). "Diurnal cycling: Observations and models of the upper ocean response to diurnal heating, cooling, and wind mixing." Journal of Geophysical Research: Oceans **91**(C7): 8411-8427.

Richardson, P. L. (1983). "Eddy kinetic energy in the North Atlantic from surface drifters." Journal of Geophysical Research: Oceans **88**(C7): 4355-4367.

Sayol, J.-M., H. Dijkstra and C. Katsman (2019). "Seasonal and regional variations of sinking in the subpolar North Atlantic from a high-resolution ocean model." Ocean Science **15**(4): 1033-1053.

Schneider, N. and P. Müller (1990). "The meridional and seasonal structures of the mixed-layer depth and its diurnal amplitude observed during the Hawaii-to-Tahiti Shuttle experiment." Journal of physical oceanography **20**(9): 1395-1404.

Seyfried, L., P. Marsaleix, E. Richard and C. Estournel (2017). "Modelling deep-water formation in the north-west Mediterranean Sea with a new air–sea coupled model: sensitivity to turbulent flux parameterizations." Ocean Science **13**(6): 1093.

Spall, M. A. (2004). "Boundary currents and watermass transformation in marginal seas." Journal of physical oceanography **34**(5): 1197-1213.

Sprintall, J., M. F. Cronin and J. T. Farrar (2018). "Upper ocean vertical structure."

Sy, A., M. Rhein, J. R. Lazier, K. P. Koltermann, J. Meincke, A. Putzka and M. Bersch (1997). "Surprisingly rapid spreading of newly formed intermediate waters across the North Atlantic Ocean." Nature **386**(6626): 675.

Thomas, L. N., J. R. Taylor, R. Ferrari and T. M. Joyce (2013). "Symmetric instability in the Gulf Stream." Deep Sea Research Part II: Topical Studies in Oceanography **91**: 96-110.

Thomson, R. E. and I. V. Fine (2003). "Estimating mixed layer depth from oceanic profile data." Journal of Atmospheric and Oceanic Technology **20**(2): 319-329.

Trowbridge, J. H. and S. J. Lentz (2018). "The bottom boundary layer." Annual review of marine science **10**: 397-420.

UNESCO, I. (1981). "Tenth report of the joint panel on oceanographic tables and standards." UNESCO Tech. Pap. Mar. Sci. **36**: 15-19.

Williams, S., M. Hecht, M. Petersen, R. Strelitz, M. Maltrud, J. Ahrens, M. Hlawitschka and B. Hamann (2011). Visualization and analysis of eddies in a global ocean simulation. Computer Graphics Forum, Wiley Online Library.